THÈSE

Presenté pour obtenir le titre de

Docteur de l'Université Louis Pasteur de Strasbourg
Images, Sciences et Technologies de l'Information
Spécialité: Photonique, Laser et Matriaux

Ecole doctorale Mathématiques, Sciences de l'Information et de l'Ingénieur

Study of Nonlinear Effects of Intense UV Beams in the Atmosphere

par

CHALUS Olivier J.

à l' Ecole Nationale Supérieure de Physique de Strasbourg

Illkirch Graffenstaden, France

Soutenue le 9 Juillet 2007 devant la commission d'examen:
Pr. Joël Fontaine, Directeur de Thèse,
Professeur à l'Institut Nationale des Sciences Appliquées de Strasbourg, France
Pr. Jean-Claude Diels, Co-Directeur de Thèse,
Professor at the University of New Mexico, USA
Pr. Charles Hirlimann, Rapporteur Interne,
Professeur, Directeur de Recherche au CNRS, Strabourg, France
Pr. Jens Biegert, Rapporteur Externe,
Professor at the Institut of Photonic Sciences of Barcelona, Spain
Dr. Alain Bourdier, Rapporteur Externe,
Commissariat à l'Energie Atomique, France
Pr. Patrick Meyrueis, Examinateur,
Professeur à l'Université de Strasbourg, France

Acknowledgments

I would like first to thanks Pr. Jean-Claude M. Diels to have accepted me in his group and support me all along my work. I would like to recognize his patience but specially his amazing knowledge in so many domains... I would like to thanks also all the members of this jury starting of course by Pr. J. Fontaine who accepted to be my advisor but also Pr. Hirlimann, Pr. Biegert, Dr. Bourdier and Pr. Meyrueis.

My regards are also going to all the members of the group: Ladan, Daniel, Jeremy, Andreas1, Andreas2, Martha, Liu Ye, Yule and Alex, but also Pr. A. Aceves and A. Sukhinin. I moreover thank Hector and every body at the CHTM and at the Physics and Astronomy Department in UNM. Special thanks are going to Ladan, Jeremy, Daniel, Martha and Andreas2 for their always passionate discussions on so many important and unimportant subjects!

Specials thanks for their support and friendship along those years are going to Debbie, Christian, John, Janot and Brent.

At last but not least, I want to deeply thanks my family: my sister and her family who always had an adventure when I go home, my brother for being myself and understanding me without any explanation, and in particular my parents for who it has been even more difficult than for me. I salute their support, their patience and their love...

Merci à tous...

.

Abstract

High intensity fs pulses have been shown to self-focus in air into filaments of typically 100 μm diameter. These fs filaments have typically energies limited to a few mJ at 800 nm, or a few tenths of mJ at 248 nm, due to a phenomenon known as "intensity clamping" [1]. This small amount of energy trapped into the short pulses filaments correlated with the energy loss during ionization prevent the beam to propagate under those conditions on a very long distance. A long distance propagation is necessary to achieve the ultimate goal of triggering, a high voltage discharge or triggering the lightning.

To be able to propagate the filament on a longer distance, more energy trapped into the filament is necessary. The theory seems to predict that a scale up of the parameters is possible in the ultraviolet. A longer pulse in time should by consequence form a more energetic filament.

Starting from the Maxwell's equation it is possible to study how the laser radiation will behave while going through the air which, if the intensity is high enough, will become a nonlinear medium. Looking for an eigenfunction solution of the equations established from the Maxwell's equations and the equation of the fluctuation of the density of electron formed by the three photon ionization, we found that the beam can propagate on a stable form. The model is valid for an initial ultraviolet pulse of a duration included between 2ns and 175ns.

The filament formed that way will have the following radial characteristics. The filament presents a central symmetry. Its diameter is predicted to be 600μm and its power about 14 times the critical power for self-focusing (P=435MW). Moreover on its profile the filament close to its center can be assimilated to a Gaussian profile. On the other hand, far from the center, on a logarithmic scale one can notice that the filament follows a linear behavior which is closer to the behavior of a Townes soliton. We can conclude from this model for the filament that it is a mix between a Gaussian profile and a Townes soliton.

The simulation of the propagation in the air can also be realized. This brings results confirming the long distance of propagation possible of long pulse ultraviolet filaments. During its propagation the filament seems to oscillate between a self-focusing phase (Kerr lensing effect) and a self-defocusing effect (plasma defocusing). The loss of power is quite consequent in the filament but it still can be sustained for a long distance (up to 5km) due to the important amount of energy trapped at the beginning. This shows that the long pulses UV filament might be the answer to trigger the lightning.

After developing a mathematical model an experimental proof is necessary. To do so, we built a high power UV source. This source consists in a Nd:YAG laser delivering 3ns pulses and 2.6J at 1064nm. The laser beam is then frequency doubled to 532nm. After the doubling of the frequency, a compression of the pulse has to be done to achieve enough power to study filamentation. The compression is realized by stimulated Brillouin scattering in FC-72. We obtain a 1.6J, 300ps pulse at 532nm. Finally another second harmonic generation allows us to achieve the UV wavelength (266nnm) were filamentation can be studied.

To be able to study the distance propagation of the filament a clear starting point for the filament is needed. To know the initial point of the filament we use an aerodynamic window which permits the focalization of the beam toward the initial conditions for the filament in the vacuum and then let the beam propagate in the air without the use of any physical window.

This setup was used to observe filament at 266nm after a propagation going from 1.5m to 4m. Their diameter is of about 400μm. The profile is close to a Gaussian. The diameter is slightly smaller than the one predicted by the theory because the pulse length is of only 200ps which does not permit to reach a steady state for the density of electron. The density of electron being smaller the defocusing effect from the plasma occur later which conclude in a smaller filament. The length of the study of the filament was limited by the size of our laboratory. Moreover some wavelengths seem to be generated during the propagation of the filament. They correspond to up to the fifth Raman Stokes of the nitrogen.

As a conclusion, we can say that we develop a mathematical model simulating the profile and the distance of propagation of long pulse UV filament. Moreover we have observed for the first time long pulse UV single filaments propagating over several meters, which represents a big step knowing that the longest pulse generating filament in air previously observed had a duration of only 2ps.

Résumé

Les impulsions de l'ordre de la femtoseconde et de haute intensités ont la capacité d'auto-focalization dans l'air en filament de diamètre de 100μm. Ces filaments ont typiquement une énergie limitée à quelques mJ à 800nm, ou quelques dizièmes de mJ à 248nm, à cause du phénomène connu comme " blocage d'intensité" [1]. La faible quantité d'énergie piègée dans les filaments d'impulsions courtes combinée avec les pertes d'énergie pendant l'ionization empêchent le faisceau de se propager dans ses conditions pour une longue distance. Une longue distance de propagation est nécessaire pour accomplir le contrôle d'une décharge électrique, ou de la foudre.

Pour être capable de se propager sur une distance plus importante il est impératif que plus d'énergie soit emmagasinée dans le filament. La théorie prédit qu'un changement d'échelle est possible dans l'ultra-violet. Une impulsion plus longue doit être capable de former un filament plus énergétique.

En partant des équations de Maxwell, il est possible d'étudier comment la radiation laser se comporte en passant dans l'air qui, si l'intensité est suffisante, agit comme un milieu nonlinéaire. Cherchant une fonction propre solution de ces équations et de l'équation décrivant la densité d'électrons formée par l'ionization à trois photons, nous trouvons que le faisceau peut se propager sous une forme stable. Ce modèle n'est valide que pour une impulsion ultra-violette de durée comprise entre 2ns et 175ns.

Le filament ainsi formé aura les caractéristiques radiales suivantes: symétrie centrale, diamètre de 600μm et puissance environ 14 fois supérieure à la puissance critiques pour auto-focalization soit 435MW. De plus, à proximité du centre du filament le profil peut être assimilé à un profile Gaussien. En revanche, au loin du centre sur une échelle logarithmique le faisceau suit une condition linéaire qui est plus proche de la description d'un soliton de Townes. Nous pouvons conclure, d'après ce modèle, que les filaments sont une combinaison d'une gaussienne et d'un soliton.

Une simulation pour la propagation dans l'air a aussi été réalisée. Les résultats

obtenus confirment qu'une longue propagation des filaments est possible pour les impulsions ultra-violettes longues. Pendant la propagation, le filament semble osciller entre une phase d'auto-focalisation (effet de Kerr) et une phase de défocalisation (plasma). Les pertes en énergie sont significatives pour les filaments mais ils peuvent tout de même être maintenus sur une longue distance (5km) par la grande quantité initiale d'énergie. Les filaments d'impulsions longues UV sont donc peut être la réponse pour le contrôle de la foudre.

Après le développement d'un modèle mathématique des preuves expérimentales sont nécessaires. C'est pourquoi nous avons construit une source haute puissance UV. Cette source consiste en un laser Nd:YAG délivrant des impulsions de 3ns et 2.6J à 1064nm. Le faisceau laser est ensuite doublé en fréquence à 532nm. Après le doublage, une compression de l'impulsion est réalisée par diffusion stimulée de Brillouin dans du FC-72. Nous obtenons ainsi 1.6J, 300ps à 532nm. Finalement un autre doublage de fréquence permet d'obtenir la longueur d'onde UV de 266nm nécessaire à l'étude de la filamentation.

Pour pouvoir étudier la distance de propagation des filaments le point de départ du phénomène doit être connu. Pour connaître ce point, nous utilisons une fenêtre aérodynamique qui permet de focaliser le faisceau dans le vide en accord avec les conditions initiales nécessaire à la filamentation.

Cette méthode a été utilisée à 266nm pour observer la propagation de filaments entre 1.5m et 4m. Leur diamètre est d'environ 400μm. Le profil est proche d'une Gaussienne. Le diamètre est légèrement plus petit que celui prédit par la théorie mais ceci peut être expliqué par la durée des impulsions laser. En effet, étant de seulement 200ps l'état stationnaire de la densité d'électrons ne peut s'établir. La densité d'électrons étant plus faible l'effet défocalisant intervient pour des filaments plus fins. La distance d'étude des filaments était limitée par la dimension du laboratoire. De plus différentes longueurs d'ondes sont créées durant la propagation des filaments. Elles correspondent aux longueurs d'onde de Stokes générées par effet Raman dans l'azote.

En conclusion, nous pouvons dire que nous avons développé un modèle mathématique pour le profil et la propagation des filaments UV à impulsions longues. Qui plus est, nous avons observé pour la première fois des filaments issus d'impulsions longues se propageant sur plusieurs mètres, ce qui représente un grand pas sachant que l'impulsion la plus longue, avant ce travail, produisant filamentation était de 2ps.

.

Contents

List of Figures

List of Tables

Chapter 1

Introduction

From being the source of fire, the expression of anger, a source of energy, lightning has always been a phenomenon that mankind wanted to control. This dream has been consistently pursued all over the history. After the cavemen, the control of the lightning was seen in the mythology in the hand of god. Zeus was able to strike the anger of the gods on anyone, which is the ultimate control of the lightning.

Closer to us in the history, come the scientist Benjamin Franklin. By sending a kite in the air with a cable attached to it, Benjamin Franklin hoped to trigger the lightning without killing himself in the process (he succeeded on both counts). Then the kite was replaced by rockets. Then the invention of the laser and progress in high power beam changed again the approach, but not the motivation.

The goal is now to create a conductive channel on the path of the laser by changing the state of the molecule using light interaction with material in hope to protect building from the power of lightning and maybe one day to store this power as a source of energy.

The first laser experiment involved in triggering the lightning came very quickly with the development of high energy laser. The first one was a CO_2 laser in the 70's [2]. The CO_2 laser, being an infrared laser, produces at high intensity some high density plasma. This plasma formed at the focus of the laser further beam

propagation. A method was designed next to create a chain of bits of plasma. A laser beam was developed, consisting in a series of concentric beams, that were focused at different distances. The bits of plasma were not optimum for the triggering of lightning: this method is not only inefficient, but also difficult to implement.

The discovery of the filamentation brought the idea of triggering the lightning with laser light into the limelight. The filament is a perfect answer of the problem of having a long ionized channel. Investigation were done at 800nm but the small distance of propagation of the infrared as filament in the air due to its important losses and avalanche ionization prevent it to be the solution for nature size experiment.

The ultraviolet wavelength seems promising because, as will be shown in this thesis, more energy can be stored for a longer time in the beam. To create such filament, a long pulse high power ultraviolet laser has to be developed.

In this dissertation the chapter 2 will treat the theory by first reviewing what is the filamentation. Then, a little study of the chemistry of the air will be done, which will lead to the establishment of a domain of validity for a model. The model for the filamentation will be introduce and some results concerning the profile of the filament and its distance of propagation will be discussed.

In the chapter 3 a presentation of the laser source with its characteristics will be made. Different problems faced during the construction of the laser will be explained. Finally the performance of the laser will be detailed.

In the chapter 4 the experimental results obtained with the laser will be shown and a comparison with the theoretical results will be discussed.

Finally, in chapter 5 we will draw the conclusion of this work and introduce some future work.

Chapter 2

Self-Focusing and -Defocusing in Air

There has been up to this work no observation of filamentation in air with pulses longer than 500 fs in the near IR and visible, nor with pulses longer than 2 ps in the UV. The fundamental reason is air breakdown in the intense field of the laser, which occurs in less than 1 ps at 800 nm. Because the mechanism of plasma heating by inverse Bremstrahlung is considerably slower for the fields present in UV filaments, it is possible to find a time scale in which the medium response to the field is stationary. It is this particular time scale that is analyzed in the first section. Next, we develop a stationary model for the spatial evolution of self-focusing and self-guiding of UV radiation in air, using a Gaussian beam approximation. In the last section, the Gaussian approximation is validated by comparing the parameters of a steady state filament with those obtained through a eigenvalue approach, by Sukhinin and Aceves [3] from the Mathematics Department at UNM.

2.1 Self-focusing

One of the most studied nonlinear phenomenon affecting the propagation of a laser beam is the self-focusing, sometimes labelled "Kerr lensing".

The wave propagating along a direction z is described by a linearly polarized field:

$$E(z,r,t) = \frac{1}{2}\tilde{\mathcal{E}}(r,z,t)e^{i(\omega t - kz)} = \frac{1}{2}\mathcal{E}e^{i(\omega t - kz + \varphi(r,z,t))}, \tag{2.1}$$

where r is the transverse coordinate (cylindrical symmetry will be assumed), and $k = 2\pi n_0/\lambda$ where n_0 is the linear index of refraction and $\lambda = 2\pi c/\omega$ is the wavelength in vacuum.

We should first consider the non-linear index of refraction of the medium in which the beam propagates, which, to first order in the intensity, can be written:

$$n = n_0 + \bar{n}_2 I \tag{2.2}$$

If the second order non-linear index of refraction of the medium is positive this could conduct to a self-focusing of the beam. The index of refraction is then described as:

$$n = n_0 + 2\bar{n}_2\sqrt{\frac{\epsilon_0}{\mu_0}}|E(\omega)|^2 \tag{2.3}$$

The index of refraction of the air depends on the intensity of the laser beam travelling through it. The index gradient is directly proportional to the intensity of the beam. Depending on the laser intensity, the nonlinear index can have a significant impact on the beam propagation.

Let us consider for instance a beam with a Gaussian intensity profile, propagating in a medium with a positive nonlinearity. According to Eq. (2.3), the beam will induce a Gaussian index profile in the medium. At a distance Δz from the beam waist, the nonlinear medium will induce a radial phase variation, which, within the paraxial approximation, can be written:

$$\varphi_{\mathrm{sf}}(r,\Delta z) = -\bar{n}_2\frac{2\pi}{\lambda}\Delta z I_0 e^{-(2r^2/w_0^2)} \approx -\bar{n}_2\frac{k}{n_0}\Delta z I_0\left(1 - 2\frac{r^2}{w_0^2}\right), \tag{2.4}$$

On the other hand, diffraction of the Gaussian beam results in a parabolic radial phase variation of opposite sign:

$$\varphi_{\mathrm{diff}}(\Delta z) = -\frac{k\Delta z}{2\rho_0^2}r^2, \tag{2.5}$$

where $\rho_0 = \pi w_0^2 n_0/\lambda$ is the Rayleigh range. The two effects balance each other when the coefficients of r^2 in Eqs. (2.4) and (2.5) are equal:

$$2\frac{\bar{n}_2 I_0}{n_0}\frac{1}{w_0^2} = \frac{1}{2}\frac{\lambda^2}{\pi^2 w_0^4 n_0^2} \tag{2.6}$$

which leads to an expression for a critical power P_{cr}:

$$P_{cr} = I_0\frac{\pi w_0^2}{2} = \frac{\lambda^2}{8\pi n_0 \bar{n}_2} \tag{2.7}$$

For any power exceeding the critical power, the diffraction is overcompensated, and the beam will collapse to a focal point. At or near the focus, some higher order nonlinear effect might dominate. These will be considered next.

2.2 Defocusing

A higher order nonlinear effect can be multiphoton ionization, if the number of photon required to ionize the medium is larger than 2. As a result of multi-photon ionization a plasma of electrons and positive ions is formed. The contribution of the electrons to the index of refraction is negative, and proportional to the square root of the concentration in electrons. It will defocuse the beam. The filament is the equilibrium between the Kerr lensing effect that focuses the beam and the plasma defocusing. The formation of the plasma and its characteristics are discussed in the next subsection.

2.2.1 Plasma Formation

The energy required to eject an electron from oxygen is 12.1eV. This free electron cloud will form the plasma. The evolution of the electron distribution following optical irradiation involves a succession of different photochemical reactions. The laser used in the experiment produce a wavelength of 266nm which correspond to a photon energy of 4.66eV. Three photons are needed to extract the electron from the oxygen.

$$O_2 + 3h\nu \rightarrow O_2^+ + e^-_{(\varepsilon=1.92eV)} \tag{2.8}$$

It has been observed that, following photoionization of oxygen, negative ions (O^-) are formed. Two different processes can contribute to this product. The first one is the simple reaction:

$$O_2 + e^- \rightarrow O^- + O. \tag{2.9}$$

For this reaction to occur the electron should present an energy of about 6.5 eV. As the electron are generated with only 1.92eV of kinetic energy, this reaction is improbable at the relatively low temperature of the plasma at its formation stage. If the plasma is heated, his two body attachment becomes dominant again when temperature exceeds 6.5 eV. A second process that result in the creation O^- at low temperature consists in a cascade of two reactions: a two photon dissociation of O_2 in 2O, followed by the attachment of the previously formed electron with one oxygen atom. This latter reaction, unlike the attachment of the electron with O_2, require only an electron with kinetic energy of 1.5 eV. The reaction sequence is:

$$O_2 + 2h\nu \rightarrow O + O \tag{2.10}$$

$$O + e^-_{(\varepsilon=1.92eV)} \rightarrow O^- + h\nu \tag{2.11}$$

Published rates for these various reactions will be used in the following chapters describing the formation of filaments. These previous measurements have been performed several decades ago in molecular beam experiments.

In the following subsection of this Chapter, some original experiments are described to verify the formation of negative oxygen ions.

2.3 Measurements on O^-

2.3.1 Absorption by a probe beam

The formation of O^- ions is at the expense of the density N_e of electrons, a key parameter in the stabilization of filaments. It is therefore desirable to find a simple

method capable of monitoring the creation of O^- ions in real time. A literature study indicates that absorption spectroscopy of O^- would be an elegant alternative. Indeed, the (single photon) photodetachment spectrum of O^- indicates an absorption cross section of $6 \cdot 10^{-18}$ cm^2 [4] in the wavelength range from 350nm to 620nm. The photodetachment reaction is:

$$O^- + h\nu \rightarrow O + e^- \tag{2.12}$$

A direct monitoring of the concentration in O^- could be performed by sending a weak probe beam through the plasma.

A recent publication by Yamaura [5] suggests that such an experiment can easily be performed. In the experiment of Yamaura, the photoionization was made with 30 ns pulses at 248 nm of 10 mJ energy, and a 2kHz repetition rate, being sent through a 1m cell filled with 1 atmosphere of dry air. The beam was slightly converging, from 20mm at the input to 10mm at the output of the cell. The probe laser beam is 5ns pulses of 5μJ at 565nm sent through the cell to probe the O^-.

These experimental conditions are to be contrasted with those described below, that include a considerably higher density and ionizing pulse energy.

In our experimental setup, a 4.5m cell filled with up to 2atm of pure oxygen (fig.2.1) is used, or a concentration in oxygen more than one order of magnitude larger than in the experiment of Yamaura [5]. The ionizing pulse is provided by the fourth harmonic (266nm) of a Nd:YAG laser, with a pulse duration of 3ns and an energy from 20 to 300mJ at 2Hz. Moreover the beam is focused in the middle of the cell after a propagation distance of about 2m. The ionizing intensity is thus more than 10^5 larger than in the experiment of Yamaura, which should result in 10^{15} times more photo-electrons. As probe beam, a CW HeNe laser at 633nm, stabilized in energy, is used. Extra care is taken to have a perfect overlap between the UV and visible focus points. The 633nm intensity is monitored at the same time as the energy of the UV pulse with detectors $D1$ and $D2$, respectively, after passing through corresponding interference filters, for two different pressures (1 and 2 atmospheres). The filter is adjusted such that the detector D_1 measures the same intensity I_0 in

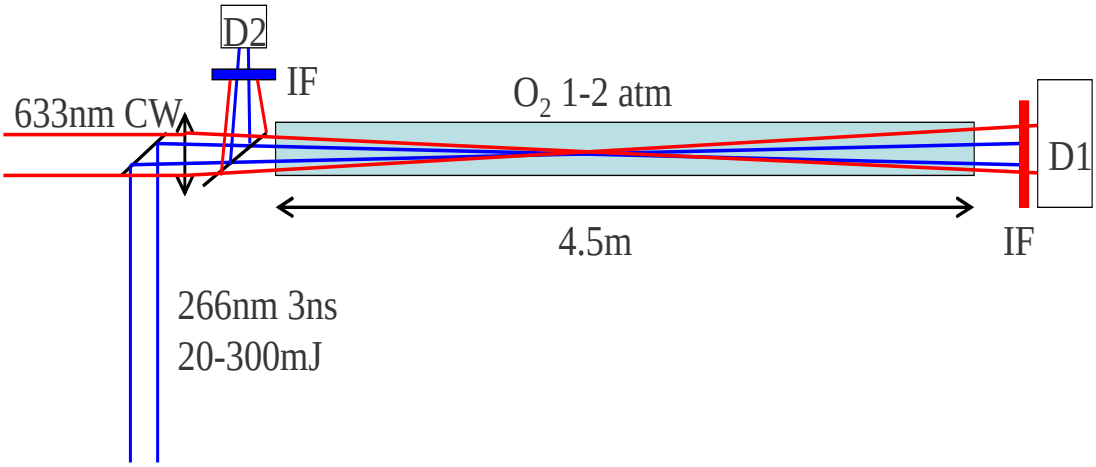

Figure 2.1: Setup for measurement of absorption by O^- (D1,2=Detector, IF=Interference filter).

the absence of UV pulse. In presence of ionizing radiation, the induced absorption coefficient $\alpha(t)$ can be recorded as a function of time:

$$\alpha(t) = -\frac{1}{L}\ln\frac{D_1}{D_2} \approx \frac{1}{L}\left(1 - \frac{D_1}{D_2}\right), \tag{2.13}$$

where L is the length of interaction region between the focused HeNe beam and the plasma. Figure 2.2 show a typical oscilloscope trace of the probe transient absorption (upper trace) indicating a 1/e decay of 620 μs. The lower trace shows the delta-function response of the detection, which has an exponential decay of 8.75 μs. The measurement is the convolution of the physical exponential decay with the response of the detection, which is also a single sided exponential. Taking the inverse Fourier transform of the ratio of the Fourier transforms of the upper to the lower traces, we find a deconvoluted response time of $\tau_o = 590\mu s$ which is the lifetime of the O^- ion.

The induced absorption, plotted versus the intensity of the UV beam, shows the expected cubic dependence (Fig 2.3). The induced absorption is also proportional to the pressure of oxygen.

The measurement of the absorption coefficient α leads directly to the concentra-

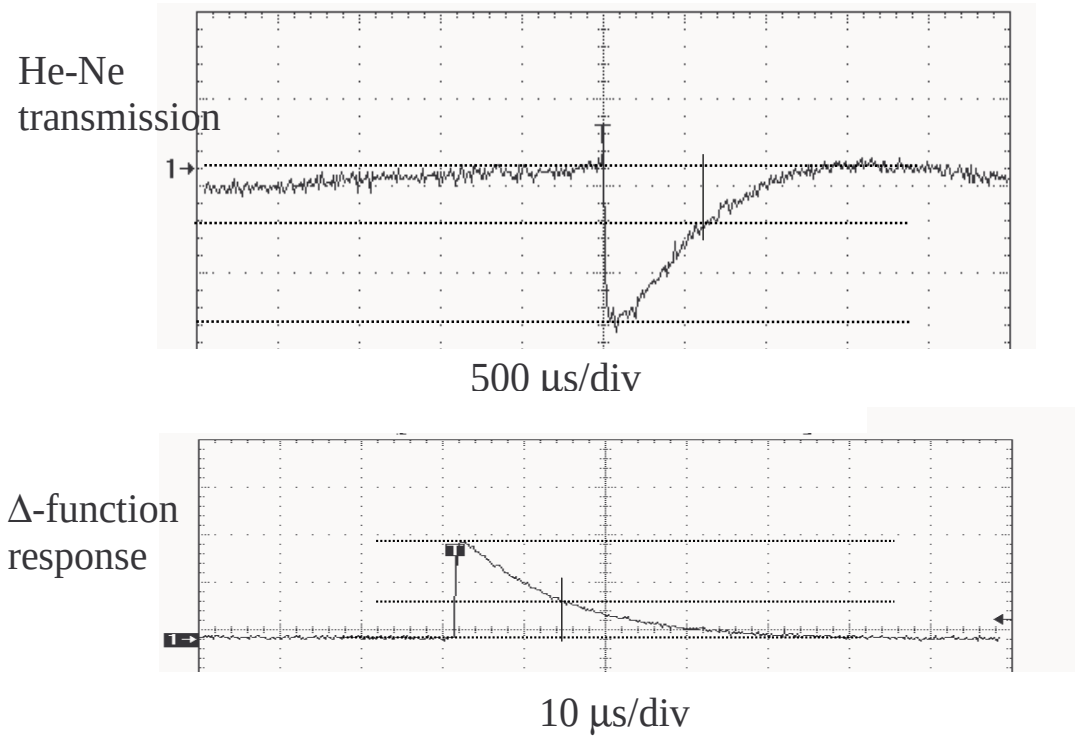

Figure 2.2: Upper trace: induced absorption on the He-Ne beam. Lower trace: δ-function response of the detector).

tion in O^- ions:

$$N_{O^-} = \frac{\alpha L}{\sigma} \tag{2.14}$$

where $\sigma = 5.8 \cdot 10^{-18}$ cm^2 is the absorption cross section of O^- at 633 nm (1.96 eV) [4].

In the following section, we use the measurement of the number of negative ions to evaluate the three photon ionization coefficient of oxygen at 266 nm.

2.3.2 Determination of the three photon ionization coefficient of O_2

At 1 atmosphere, with an ionizing laser power of 10MW (intensity of 2.5×10^{15}W/m^2), an attenuation of 34% of the probe He-Ne laser is measured. This leads to an estimate

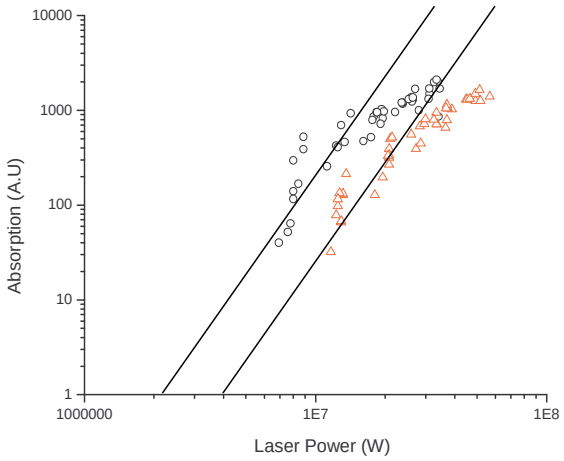

Figure 2.3: Absorption at 633nm induced by the recombination of electrons with oxygen. The absorption coefficient is proportional to the concentration in O^- ions. Circles: 2 atm pressure, Triangles: 1 atm pressure. The straight lines indicate the slope correspond to the (power)^3.

of $N_{O^-} = 5.6 \times 10^{22}\mathrm{m}^{-3}$ for the density of O^-.

The density of generated electron follows the equation:

$$\frac{dN_e}{dt} = \sigma^{(3)} N_{O_2} I^3. \tag{2.15}$$

In a steady state situation, after a long enough interaction time one can approximate:

$$N_{O^-} \approx \sigma^{(3)} N_{O_2} I^3 \tau_l \tag{2.16}$$

where τ_l is the pulse duration of the ionizing laser, N_{O_2} the density of oxygen in the cell, I the intensity of the ionizing laser and $\sigma^{(3)}$ the three photon ionization coefficient. Approximating the beam profile with a Gaussian, the intensity is:

$$I = \frac{2P}{\pi w_0^2} \tag{2.17}$$

where w_0 is the $1/e$ half-with of the beam (waist) and P the power of the laser.

Finally, combining the equations 2.14, 2.14 and 2.17, one can extract:

$$\sigma^{(3)} = \frac{\alpha L}{\tau_l \sigma N_{O_2}} \left(\frac{\pi w_0^2}{2P} \right)^3. \tag{2.18}$$

From the equation 2.18, the three photon ionization coefficient for oxygen is evaluated to be $\sigma^{(3)} = 4.1 \times 10^{-41}\mathrm{m}^6\mathrm{s}^2/\mathrm{J}^3$.

2.3.3 Comparison with the measurements of Yamaura

The measurements were also attempted with a 1cm collimated beam under 2atm of pure oxygen. Those conditions where more favorable than the one of Yamaura [5] (pure oxygen, higher pressure, longer cell, ten times more energy per pulses, pulses ten times shorter) but no signal was detected ·

It should be noted that the experiments of Yamaura were performed at a pulse period of 500 μs, which implies an enhancement factor f of:

$$f = \frac{1}{1 - e^{-T/\tau_o}} = 1.75. \tag{2.19}$$

It does therefore remains a mystery how the results of Yamaura were obtained.

2.4 Domain of Validity of a stationary medium response

The domain of validity of a stationary model will be sandwiched between two limits: the lower bound as determined by the transient response, and an upper bound set by an avalanche breakdown effect.

2.4.1 Lower limit: end of the transient response

The density of electron in the beam path should reach an equilibrium value between the creation of electrons by three photon ionization, and the disappearance by recombination and attachment to oxygen. The evolution of the electrons N_e follows the equation:

$$\frac{dN_e}{dt} = \sigma^{(3)} N_{O_2} I^3 - \beta_{ep} N_{O_2}^2 - \gamma N_e. \tag{2.20}$$

In this equation $\sigma^{(3)}$ corresponds to the three photon ionization coefficient of oxygen, N_O the density of oxygen molecules in air, I the intensity of the ionizing laser beam,

β_{ep} the recombination factor and γ the two body attachment coefficient to oxygen. In this equation the diffusion of the electrons can be neglected. Indeed, according to Hegerberg [6], the diffusion coefficient is of the order of $10^{21}\mathrm{cm}^{-1}\mathrm{s}^{-1}$ which brings at 1 atmosphere and for a time duration of 200ns a diffusion of the electron of about 40μm. This distance is 10 times smaller than the minimum expected filament size. We can therefore consider the diffusion of electrons in the plasma to have a negligible impact on the plasma density. In the absence of an applied electric field, the drift of the electron can be completely neglected.

Photoionization

We chose a value of $3\times10^{-41}\mathrm{m}^6\mathrm{s}^2\mathrm{J}^{-3}$ for $\sigma^{(3)}$, consistent with published experimental data [7, 8], and our own data previously presented $4.1\times10^{-41}\mathrm{m}^6\mathrm{s}^2\mathrm{J}^{-3}$. Among other experimental and theoretical values in the literature that span four orders of magnitude, this is the only experimental value matching a theoretical value calculated from the Keldysh [9]

Recombination

The recombination coefficient is taken from the extrapolation of the data from Biondi [10] reproduced in Fig. 2.4. At higher temperatures, the coefficient of recombination tends to scale up in $c_r\times\mathrm{T}_e^{-0.5}$ We fixed c_r to match the higher temperature point on the figure to obtain:

$$\beta_{ep} \approx 2.3 \times 10^{-12} T_e^{-0.5} \tag{2.21}$$

where T_e is taken in Kelvin. This bring us to a value for $\beta_{ep} = \approx 1.3 \times 10^{-14}\mathrm{m}^3\mathrm{s}^{-1}$.

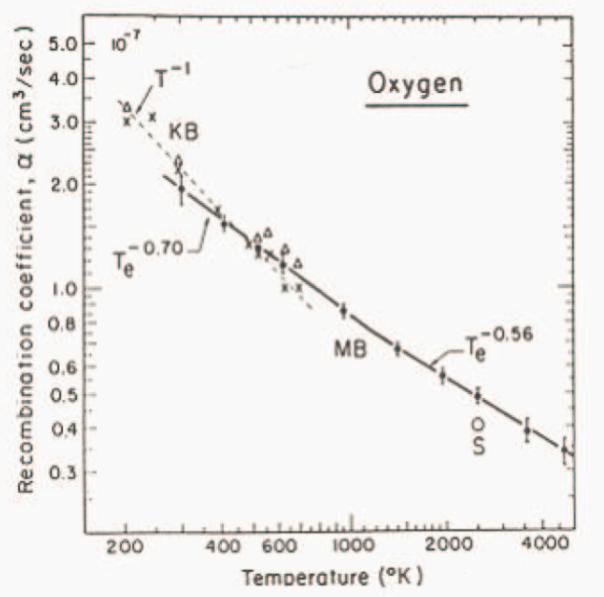

Figure 2.4: Experimental measurement of the recombination coefficient.

Attachment

There are several reaction paths by which an electron is attached to an oxygen atom. As mentioned in the beginning of this chapter, the simple reaction

$$O_2 + e^- \rightarrow O^- + O \tag{2.22}$$

will not be considered because it requires electron energies higher than 6.5eV [1]. Instead, the attachment of electron to oxygen proceeds by the two successive reactions given previously Eqs. (2.10 2.11). The contribution to the decay of electron population can be written:

$$\frac{dN_e}{dt} = -\eta_{att}[O_2]N_e, \tag{2.23}$$

where $[O_2]$ is the concentration of oxygen and η_{att} is given by [11]:

$$\eta_{att} = 2.75 \times 10^{-10} T_e^{-0.5} e^{-\frac{5}{T_e}} cm^3 s^{-1} \tag{2.24}$$

where T_e is the temperature of the electrons expressed in eV. We get $\gamma = \eta_{att}[O_2]$. Figure 2.5 shows γ as a function of the electron temperature.

[1] This reaction may become a factor at the late end of the domain validity mode, when the electron plasma has been heated to 6.5 eV. It will serve to cool the plasma, and may

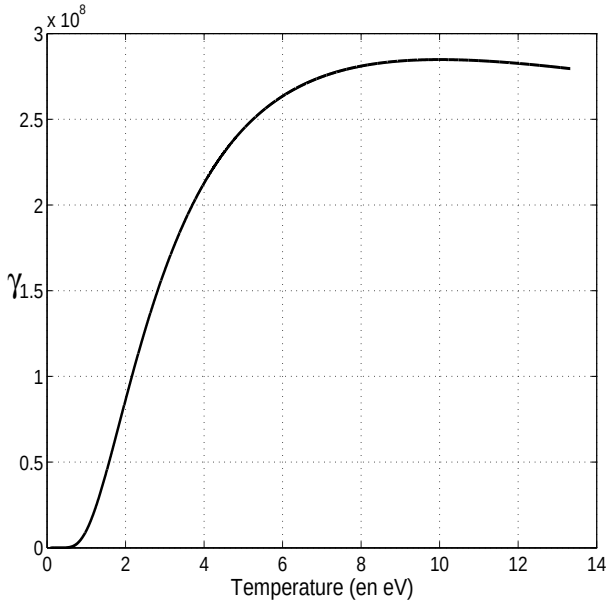

Figure 2.5: Attachment coefficient as a function of the electron temperature.

To verify our scaling law we compared our simulation to experimental results [12] when temperatures over 2eV are considered (Fig. 2.6). To do so we have calculated the attachment cross-section:

$$\sigma = \frac{[O_2]}{[air]} \frac{V_T}{\eta_{att}} \tag{2.25}$$

where V_T is the speed of the particles that recombine and [air] is the density of the air.

Three body attachment reactions can also be considered for producing negative oxygen ions. The reaction taking place in those cases are the following:

$$e^- + O_2 + N_2 \rightarrow O_2^- + N_2 \tag{2.26}$$

$$e^- + O_2 + O_2 \rightarrow O_2^- + O_2 \tag{2.27}$$

If we plot the values of those three body cross-section in comparison of the two body cross-section, we can see that for electron temperature over 1 eV the two body cross-section dominates the other ones, and can even be more than two orders of

even extend the upper time limit of validity of the stationary model.

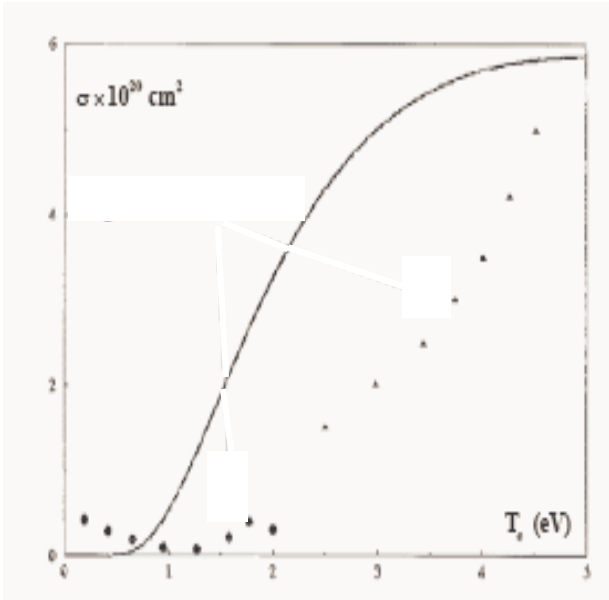

Figure 2.6: Two body attachment cross-section. Experimental data points [12] compared to our simulation.

magnitudes higher (Fig. 2.7). This allows us to neglect the three body attachment in the calculation of the density of electrons present in the beam path.

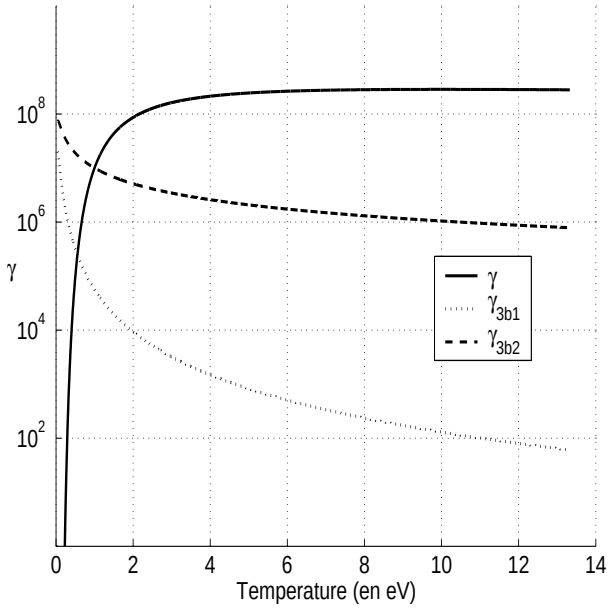

Figure 2.7: The two body attachment factor is dominant in comparison of the three body factors for temperature over 1eV.

Initial transient

All the parameters of Eq. (2.20) having been established in the previous subsections, one can proceed with a numerical solution. Figure 2.8 shows the evolution of the density of electron as a function of time, for a step function ($I = 5 \cdot 10^1 1$ W/cm^2) ionizing laser. We can see that N_e join a stable value N_{eq}. This value can be expressed

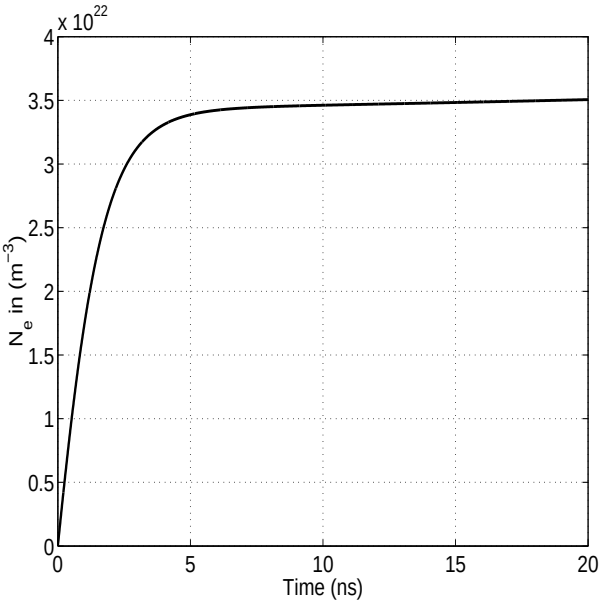

Figure 2.8: Evolution of the density of electron in function of time. A step function pulse of $5 \cdot 10^{11}$ W/cm^2 intensity is assumed.

by:

$$N_{eq} = \frac{-\gamma + \sqrt{\gamma^2 + 4\beta_{ep} N_{O_2} \sigma^{(3)} I^3}}{2\beta_{ep}} \tag{2.28}$$

75% of this value is obtained after 2ns. We can consider the domain of validity of our model to start at a pulse duration over 2ns.

2.4.2 Upper limit: onset of avalanche

The upper limit to the domain of validity of the steady state approach is set by avalanche ionization. The electrons are heated by inverse Bremsstrahlung. When

they reach a temperature that is higher than the ionization energy of oxygen (12.2eV) avalanche ionization occurs. The evolution of the temperature of the electrons function of laser pulse duration is plotted in figure 2.9.

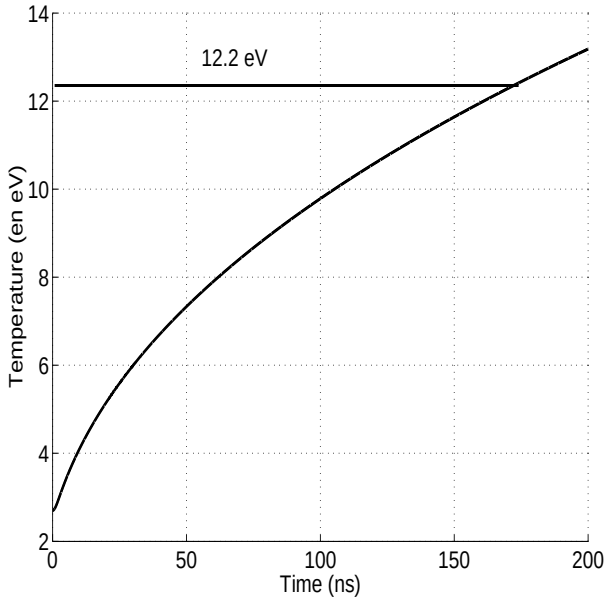

Figure 2.9: Evolution of the temperature of the electrons in function of time. A step function pulse of $5 \cdot 10^1 1$ W/cm^2 intensity is assumed.

One can see that the temperature of 12.2eV is not achieved before a pulse duration of about 175ns.

We can finally say that the domain of validity of our model is situated for ionizing laser pulse duration between 2ns and 175ns.

2.5 Beam evolution with distance (Gaussian beam approximation)

2.5.1 Townes Soliton

We start with Maxwell's equation:

$$\left[\Delta_{tr} + \partial_{zz}^2 - \frac{n_0^2}{c^2}\partial_{tt}^2\right]\frac{1}{2}\tilde{\mathcal{E}}e^{i(\omega t - kz)} = \mu_0 \partial_{tt}^2 P_{NL}. \tag{2.29}$$

We consider particular experimental conditions in which the nonlinear polarization $P_{NL} = (1/2)\tilde{\mathcal{P}}\exp(i(\omega t - kz))$ can be considered to be stationary. This is for instance the case when only the Kerr nonlinearity is involved:

$$\mu_0 \partial_{tt}^2 P_{NL} = -\frac{1}{2}\frac{\omega^2}{c^2}\chi^{(3)}|\tilde{\mathcal{E}}|^2\tilde{\mathcal{E}} \tag{2.30}$$

Consistent with the stationarity condition $\partial_{tt}^2 \to -\omega^2$, and, in the case of cylindrical symmetry, Eq. (2.29) reduces to:

$$\begin{aligned}
2ik\partial_z\tilde{\mathcal{E}} &= \partial_{rr}^2\tilde{\mathcal{E}} + \frac{1}{r}\partial_r\tilde{\mathcal{E}} + \frac{\omega^2}{c^2}\chi^{(3)}|\tilde{\mathcal{E}}|^2\tilde{\mathcal{E}} \\
2ik\partial_z\tilde{\mathcal{E}} &= \partial_{rr}^2\tilde{\mathcal{E}} + \frac{1}{r}\partial_r\tilde{\mathcal{E}} + \frac{\omega^2}{c^2}2n_0\bar{n}_2 I\tilde{\mathcal{E}} \\
2ik\partial_z\tilde{\mathcal{E}} &= \partial_{rr}^2\tilde{\mathcal{E}} + \frac{1}{r}\partial_r\tilde{\mathcal{E}} + \frac{4\pi^2 n_0^2}{\lambda^2}\frac{\bar{n}_2|\mathcal{E}|^2}{\eta_0}\tilde{\mathcal{E}} \\
2ik\partial_z\tilde{\mathcal{E}} &= \partial_{rr}^2\tilde{\mathcal{E}} + \frac{1}{r}\partial_r\tilde{\mathcal{E}} + k^2\frac{\bar{n}_2|\mathcal{E}|^2}{\eta_0}\tilde{\mathcal{E}}
\end{aligned} \tag{2.31}$$

In Eq. (2.31) $\tilde{\mathcal{E}} = \tilde{\mathcal{E}}(z, r)$ is the complex electric field envelope, $\eta_0 = \sqrt{\mu_0/\epsilon_0} = 377$ Ohms the characteristic impedance of vacuum. The phase part of that function describes the phasefront of the field.

Alternative approach

We can derive the same set of Eqs. (2.31) by including the nonlinear index in the $k-$vector, and writing for Maxwell's equations simply:

$$\left[\Delta_{tr} + \partial_{zz}^2 - \frac{n^2}{c^2}\partial_{tt}^2\right]\frac{1}{2}\tilde{\mathcal{E}}e^{i(\omega t - kz)} = 0. \tag{2.32}$$

in which the index of refraction includes the nonlinear part:

$$n = n_0 + \bar{n}_2 I. \tag{2.33}$$

Performing the derivation in Eq. (2.32), we find:

$$2ik\partial_z \tilde{\mathcal{E}} = \partial_{rr}^2 \tilde{\mathcal{E}} + \frac{1}{r}\partial_r \tilde{\mathcal{E}} + \frac{\omega^2}{c^2} 2n_0 \bar{n}_2 I \tilde{\mathcal{E}}. \tag{2.34}$$

consistent with Eq. (2.31)

Nonlinear Schrödinger equation

One approach to the solution is to use a Gaussian approximation, leading to a wave-front that can be approximated by a spherical (parabolical) surface on axis. A *steady state* solution however is necessarily a *plane wave*; hence an electrical field envelope of the form:

$$\tilde{\mathcal{E}} = \mathcal{E}_s e^{-ik_s z} \tag{2.35}$$

where $\mathcal{E}_s(r)$ is the soliton profile, and k_s a correction to the wave vector k. Substituting in Eq. (2.31):

$$2kk_s\mathcal{E}_s = \partial_{rr}^2 \mathcal{E}_s + \frac{1}{r}\partial_r \mathcal{E}_s + k^2 \frac{\bar{n}_2}{\eta_0} \mathcal{E}_s^3 \tag{2.36}$$

We get to the dimensionless soliton equation by dividing both sides by k^2, and defining the dimensionless transverse variable $\chi = r/r_0$ where

$$r_0 = \frac{1}{k} \tag{2.37}$$

The problem has also a characteristic field given by:

$$\boxed{\mathcal{E}_0 = \sqrt{\frac{\eta_0}{\bar{n}_2}}} \tag{2.38}$$

Finally, $\beta = 2k_s/k$ is the eigenvalue of the nonlinear Schrödinger equation:

$$\beta \mathcal{E}_r = \partial_{\chi\chi}^2 \mathcal{E}_r + \frac{1}{\chi}\partial_\chi \mathcal{E}_r + \mathcal{E}_r^3 \tag{2.39}$$

where the "wave function" $\mathcal{E}_r = \mathcal{E}/\mathcal{E}_0$. The corresponding normalized propagation equation (to be used in the Gaussian approximation) takes the form:

$$2i\frac{\partial}{\partial(kz)}\left(\frac{\tilde{\mathcal{E}}}{\mathcal{E}_0}\right) = \partial_{\chi\chi}^2\left(\frac{\tilde{\mathcal{E}}}{\mathcal{E}_0}\right) + \frac{1}{\chi}\partial_\chi\left(\frac{\tilde{\mathcal{E}}}{\mathcal{E}_0}\right) + \left(\frac{\tilde{\mathcal{E}}}{\mathcal{E}_0}\right)^3. \tag{2.40}$$

2.5.2 Higher order terms – coarse approximation

The production/decay of the electron density N_e evolves according to:

$$\frac{dN_e}{dt} = \sigma^{(n)} I^n N_o - \beta_{ep} N_e^2 - \gamma N_e, \tag{2.41}$$

where $\sigma^{(n)}$ is the n^{th} order multiphoton ionization coefficient, I the intensity of the laser beam, $\beta_{ep} \approx 2.3 \times 10^{-12} T_e^{-0.5}$ is the electron-positive-ion recombination coefficient where the electron temperature T_e is expressed in Kelvin, and γ the electron oxygen attachment coefficient. The attachment coefficient to oxygen, at an electron temperature of 2.7 eV, is $\gamma = 1.5 \cdot 10^8$ s^{-1} [11]. The ionization coefficient $\sigma^{(3)}$ for the oxygen is taken to be 3.0×10^{-29}cm^{6}s^{2}J^{-3}. The density of electron join a stable level after about 2ns. To be in steady state solution the electron temperature should stay under 12.2eV to prevent inverse Bremsstrahlung to occur, which involve a maximum pulse duration of 175ns.

For the case of three photon ionization ($n = 3$), steady state solution for Eq. (2.41) is:

$$\begin{aligned} N_e &= \frac{\sqrt{\gamma^2 + 4\sigma^{(3)} I^3 N_0 \beta_{ep}} - \gamma}{2\beta_{ep}} \\ &\approx \frac{\sqrt{4\sigma^{(3)} I^3 N_0 \beta_{ep}}}{2\beta_{ep}}\left[1 + \frac{1}{2}\frac{\gamma^2}{4\sigma^{(3)} I^3 N_0 \beta_{ep}}\right] - \frac{\gamma}{2\beta_{ep}} \end{aligned} \tag{2.42}$$

Since it contains no field dependence, the last term of the development contributes only to the linear polarization, and can thus be ignored. We will neglect the second term in the bracket for being small compared to unity. The remaining term in the expression for the steady state value of N_e is thus proportional to the third power of the field amplitude.

The corresponding nonlinear polarization amplitude is

$$\tilde{\mathcal{P}}_{NL} = \epsilon_0 \frac{\omega_p^2}{\omega^2}\tilde{\mathcal{E}} = \frac{\epsilon_0}{\omega^2}\frac{N_e e^2}{m_e \epsilon_0}\tilde{\mathcal{E}}, \tag{2.43}$$

were ω_p is the plasma frequency, m_e the electron mass. Including the additional term on the right-hand side of Eq. (2.31):

$$2ik\partial_z\tilde{\mathcal{E}} = \partial_{rr}^2\tilde{\mathcal{E}} + \frac{1}{r}\partial_r\tilde{\mathcal{E}} + k^2\frac{\bar{n}_2|\mathcal{E}|^2}{\eta_0}\tilde{\mathcal{E}} - \frac{\omega^2}{c^2}\frac{\omega_p^2}{\omega^2}\tilde{\mathcal{E}} \tag{2.44}$$

Substituting in the plasma frequency the expression for the photoelectron density, the last equation becomes:

$$2ik\partial_z\tilde{\mathcal{E}} = \partial_{rr}^2\tilde{\mathcal{E}} + \frac{1}{r}\partial_r\tilde{\mathcal{E}} + k^2\frac{\bar{n}_2|\mathcal{E}|^2}{\eta_0}\tilde{\mathcal{E}} - k^2\frac{\mathcal{E}^3}{\mathcal{E}_c^3}\tilde{\mathcal{E}} \tag{2.45}$$

where we have defined a characteristic electric field amplitude $\mathcal{E}_c$ relating to the plasma production:

$$\frac{1}{\mathcal{E}_c^3} = \frac{e^2 c}{2m_e\omega^2}\sqrt{\frac{\sigma^{(3)}N_0}{2\eta_0\beta_{ep}n_0}} \tag{2.46}$$

The complete equation can thus be put in dimensionless form:

$$2i\frac{\partial}{\partial(kz)}\left(\frac{\tilde{\mathcal{E}}}{\mathcal{E}_0}\right) = \partial_{\chi\chi}^2\left(\frac{\tilde{\mathcal{E}}}{\mathcal{E}_0}\right) + \frac{1}{\chi}\partial_\chi\left(\frac{\tilde{\mathcal{E}}}{\mathcal{E}_0}\right) + \left(\frac{\mathcal{E}}{\mathcal{E}_0}\right)^2\left(\frac{\tilde{\mathcal{E}}}{\mathcal{E}_0}\right) - \left(\frac{\mathcal{E}_0}{\mathcal{E}_c}\right)^3\left(\frac{\mathcal{E}}{\mathcal{E}_0}\right)^3\frac{\tilde{\mathcal{E}}}{\mathcal{E}_0} \tag{2.47}$$

The eigenvalue equation, using the same notations as for Eq. (2.39), and using $\beta = 2k_s/k$ as the eigenvalue of the new nonlinear equation:

$$\beta\mathcal{E}_r = \partial_{\chi\chi}^2\mathcal{E}_r + \frac{1}{\chi}\partial_\chi\mathcal{E}_r + \mathcal{E}_r^3 - a\mathcal{E}_r^4 \tag{2.48}$$

where $a = (\mathcal{E}_0/\mathcal{E}_c)^3$ represents the relative strength of the Kerr effect to the ionization.

An intermediate step

Substituting the relevant approximation from Eq. (2.42) in Eq. (2.43), we find that the coefficient of $k^2 = 2\pi n_0/\lambda$ in the last term of the right hand side of Eq. (2.45) is:

$$\begin{aligned} & \frac{1}{n_0^2}\frac{e^2}{m_e\epsilon_0\omega^2}\sqrt{\frac{\sigma^{(3)}I^3N_0}{\beta_{ep}}}\tilde{\mathcal{E}} \\ = & \frac{e^2}{m_e\omega^2}\mathcal{E}^3\sqrt{\frac{\sigma^{(3)}n_0^3N_0}{8\frac{\mu_0}{\epsilon_0}\sqrt{\frac{\mu_0}{\epsilon_0}}\beta_{ep}n_0^4\epsilon_0^2}}\tilde{\mathcal{E}} \\ = & \frac{e^2}{2m_e\omega^2}\mathcal{E}^3\sqrt{\frac{\sigma^{(3)}N_0}{2\mu_0\epsilon_0\eta_0\beta_{ep}n_0}}\tilde{\mathcal{E}} \\ = & \frac{e^2c}{2m_e\omega^2}\mathcal{E}^3\sqrt{\frac{\sigma^{(3)}N_0}{2\eta_0\beta_{ep}n_0}}\tilde{\mathcal{E}} \end{aligned} \tag{2.49}$$

The above was a bad approximation. It does give however a more "elegant", simpler Schrödinger equation, valid only for negligible attachment of electron to oxygen. In the next section we use the complete steady state solution of the differential equation for the electron density Eq. (2.41)

2.5.3 Taking into account the electron attachment to oxygen

Neglecting the attachment to oxygen is not a good approximation. One can use directly the exact solution for N_e [first line of Eq. (2.42)] in the expression (2.43) for the polarization. To an electron density N_e corresponds a nonlinear polarization amplitude:

$$\tilde{\mathcal{P}}_{NL} = \epsilon_0\frac{\omega_p^2}{\omega^2}\tilde{\mathcal{E}} = \frac{\epsilon_0}{\omega^2}\frac{N_e e^2}{m_e\epsilon_0}\tilde{\mathcal{E}}, \tag{2.50}$$

were ω_p is the plasma frequency, m_e the electron mass. Including the additional term on the right-hand side of Eq. (2.31):

$$2ik\partial_z\tilde{\mathcal{E}} = \partial_{rr}^2\tilde{\mathcal{E}} + \frac{1}{r}\partial_r\tilde{\mathcal{E}} + k^2\frac{\bar{n}_2|\mathcal{E}|^2}{\eta_0}\tilde{\mathcal{E}} - \frac{\omega^2}{c^2}\frac{\omega_p^2}{\omega^2}\tilde{\mathcal{E}} \tag{2.51}$$

The coefficient of $k^2 = \omega^2 n_0^2/c^2$ in the last term of the propagation equation (2.51) is:

$$\begin{aligned} -\frac{\omega_p^2}{n_0^2\omega^2} &= -\frac{N_e e^2}{m_e \epsilon_0 n_0^2 \omega^2} \\ &= -\frac{e^2}{m_e \epsilon_0 n_0^2 \omega^2} \left\{ \sqrt{\left(\frac{\gamma}{2\beta_{ep}}\right)^2 + \frac{\sigma^{(3)} N_0 I^3}{\beta_{ep}}} - \left(\frac{\gamma}{2\beta_{ep}}\right) \right\} \\ &= -\sqrt{A^2 + B^2 \mathcal{E}_r^6} + A \end{aligned} \tag{2.52}$$

where A and B are the dimensionless quantities:

$$\boxed{A = \frac{e^2}{2m_e\omega^2} \frac{\gamma}{\beta_{ep} n_0^2 \epsilon_0}} \tag{2.53}$$

and

$$\boxed{B^2 = \left(\frac{e^2}{m_e\omega^2}\right)^2 \frac{\sigma^{(3)} c^2 N_0 \mathcal{E}_0^6}{8\eta_0 \beta_{ep} n_0}} \tag{2.54}$$

Maxwell's equation, in dimensionless form, becomes now:

$$2i \frac{\partial}{\partial(kz)} \tilde{\mathcal{E}}_r = \partial_{\chi\chi}^2 \tilde{\mathcal{E}}_r + \frac{1}{\chi} \partial_\chi \tilde{\mathcal{E}}_r + \mathcal{E}_r^2 \tilde{\mathcal{E}}_r - \left(\sqrt{A^2 + B^2 \mathcal{E}_r^6} - A \right) \tilde{\mathcal{E}}_r. \tag{2.55}$$

A *steady state* solution is necessarily a *plane wave*; hence an electrical field envelope of the form:

$$\tilde{\mathcal{E}}_r = \tilde{\mathcal{E}}_s e^{-ik_s z} \tag{2.56}$$

where $\tilde{\mathcal{E}}_s(\chi)$ is the normalized soliton profile, and k_s a correction to the wave vector k. Substituting in Eq. (2.55):

$$\beta \tilde{\mathcal{E}}_s = \partial_{\chi\chi}^2 \tilde{\mathcal{E}}_s + \frac{1}{\chi} \partial_\chi \tilde{\mathcal{E}}_s + \mathcal{E}_s^2 \tilde{\mathcal{E}}_s - \left(\sqrt{A^2 + B^2 \mathcal{E}_s^6} - A \right) \tilde{\mathcal{E}}_s, \tag{2.57}$$

where $\beta = 2k_s/k$ is the eigenvalue of the nonlinear Schrödinger equation.

Power loss

There are two loss mechanisms to take into account: the power loss due to three photon ionization of oxygen (dominant one) and the power loss due to plasma absorption.

Let us assume for now that the plasma absorption is negligible. Expressing that the three photon used for ionization result in beam depletion:

$$\frac{dI}{dz} = -3\hbar\omega \left(\frac{dN_e}{dt}\right)_{\text{3photon absorption}} = -3\hbar\omega\sigma^{(3)}N_0 I^3. \tag{2.58}$$

Power loss in the Gaussian approximation

In the simplify model that follows, it will be assumed that the shape of the profile remains a Gaussian. The power of the Gaussian beam is:

$$P = \frac{\pi w^2}{2} I = \frac{\pi w^2}{2} \cdot \frac{n_0 \mathcal{E}^2}{2\eta_0} \tag{2.59}$$

Differentiating:

$$dP = 2\frac{dw}{w}P + 2P\frac{d\mathcal{E}}{\mathcal{E}}. \tag{2.60}$$

In absence of absorption, the power is conserved, and the change in field amplitude due to a change in beam width is:

$$d\mathcal{E} = -\frac{\mathcal{E}}{w}dw. \tag{2.61}$$

Combining with Eq. (2.58) and using the normalization to k for the distance:

$$\boxed{\frac{d\tilde{\mathcal{E}}}{dkz} = -\frac{3\hbar\omega\sigma^{(3)}N_0 n_0^2}{8k\eta_0^2}\tilde{\mathcal{E}}^{*2}\tilde{\mathcal{E}}^2\tilde{\mathcal{E}} - \frac{\mathcal{E}}{w}\frac{dw}{d(kz)}} \tag{2.62}$$

Here again, we can define a characteristic field $\mathcal{E}_{\text{3ph}}$,

$$\frac{1}{\mathcal{E}_{\text{3ph}}^4} = \frac{3\hbar\omega\sigma^{(3)}N_0 n_0^2}{8k\eta_0^2} \tag{2.63}$$

to re-write Eq. (2.47) in the dimensionless form:

$$\frac{\partial\mathcal{E}_r}{kz} = -\frac{1}{c^4}|\mathcal{E}_r|^4\mathcal{E}_r - \mathcal{E}_r\frac{1}{w}\frac{dw}{d(kz)} \tag{2.64}$$

where $c = \mathcal{E}_{3\mathrm{ph}}/\mathcal{E}_0$ is the characteristic field for three photon absorption, and the normalized field is $\mathcal{E}_r = \tilde{\mathcal{E}}/\mathcal{E}_0$.

Numerical values of those parameters are presented in the Appendix B

2.5.4 Gaussian Approximation

First approach: neglecting oxygen attachment

Let us first consider the lossless situation ($b = 0$), and insert the Gaussian ansatz:

$$\tilde{\mathcal{E}}_r(kz,\chi) = \frac{w_0}{w(kz)}\tilde{\mathcal{E}}_{r,0}e^{-\chi^2/w(kz)^2}e^{-i\frac{\chi^2}{2R}-i\varphi(kz)} \tag{2.65}$$

where the phase factor on axis $\varphi(kz)$, the *normalized* beam size $w(kz)$ and the *normalized* wavefront curvature $R(kz)$ are all quantities linked to each other by Maxwell's equation. With the nonlinear propagation equation (2.64), we no longer have the relation that $\varphi(z) = -\arctan(kz/kz_0)$ where kz_0 is the *normalized* Raleigh range. The relation between these functions will result from the substitution of Eq. (2.65) into the propagation equation (2.64), separating real and imaginary parts, and identifying terms of the same order in (χ^2/w^2). In the following we will write w instead of $w(kz)$ and R instead of $R(kz)$ for convenience. We perform the three spatial derivatives on the Gaussian beam (2.65) that will have to be substituted in Eq. (2.64):

$$\begin{aligned}
2i\frac{\partial\tilde{\mathcal{E}}_r}{\partial kz} &= \left[-\frac{1}{w}\frac{dw}{dkz} - i\frac{\chi^2}{2}\frac{d}{dkz}\frac{1}{R} - i\frac{d}{dkz}\varphi(kz) + \frac{2\chi^2}{w^3}\frac{dw}{dkz}\right]\tilde{\mathcal{E}}_r \\
\frac{1}{\chi}\frac{\partial\tilde{\mathcal{E}}_r}{\partial\chi} &= \left(-i\frac{1}{R} - \frac{2}{w^2}\right)\tilde{\mathcal{E}}_r \\
\frac{\partial^2\tilde{\mathcal{E}}_r}{\partial\chi^2} &= \left[\left(-i\frac{1}{R} - \frac{2}{w^2}\right) - \left(\frac{\chi}{R}\right)^2 + i\frac{4\chi^2}{Rw^2} + \frac{4\chi^2}{w^4}\right]\tilde{\mathcal{E}}_r
\end{aligned} \tag{2.66}$$

Substituting into Eq. (2.64) yields the following real and imaginary parts:

$$2\left[\frac{d}{dkz}\varphi(kz) + \frac{\chi^2}{2}\frac{d}{dkz}\frac{1}{R}\right] = -\frac{4}{w^2} - \frac{\chi^2}{R^2} + \frac{4\chi^2}{w^4} + \mathcal{E}_r^2 - a\mathcal{E}_r^3 \tag{2.67}$$

$$2\left[-\frac{1}{w}\frac{dw}{dkz} + \frac{2\chi^2}{w^3}\frac{dw}{dkz}\right] = \frac{4\chi^2}{Rw^2} - \frac{2}{R} \tag{2.68}$$

Considering a beam on axis ($r = 0$) and ignoring both the Kerr effect and the plasma defocusing, we can verify the linear limit of Eq. (2.67) for the linear approximation (taking into account the diffraction equation for a Gaussian beam $w = w_0(1 + z^2/z_0^2)^{1/2}$):

$$\frac{d}{dkz}\varphi(z) = -2\frac{1}{w_0^2(1+z^2/z_0^2)} = -\frac{1/z_0}{1+z^2/z_0^2} = -\frac{d}{dz}\arctan\frac{z}{z_0}. \tag{2.69}$$

which is the standard expression for a Gaussian beam. Note that, in the dimensionless units that we chose, $kz_0 = w_0^2$.

Looking at the terms in Eq. (2.68) that are of zero and first order in r^2/w^2 we find:

$$\frac{1}{R} = \frac{1}{w}\frac{dw}{dkz} \tag{2.70}$$

We note that this last term simply states the physical relation between the broadening of the beam and the wavefront curvature. Before we separate Eq. (2.67) into zero and first order terms in r^2/w^2 we make the parabolic approximation for the electric field near the beam axis so that:

$$\frac{w_0}{w}\mathcal{E}_{r,0}e^{-\frac{\alpha r^2}{w^2}} \approx \frac{w_0}{w}\mathcal{E}_{r,0}\left(1-\alpha\frac{r^2}{w^2}\right). \tag{2.71}$$

For the zero order terms in Eq. (2.67) we get:

$$2\frac{d}{dkz}\varphi(kz) = \frac{w_0^2}{w^2}\mathcal{E}_{r,0}^2\left[1-a\frac{w_0}{w}\mathcal{E}_{r,0}\right] - \frac{4}{w^2} \tag{2.72}$$

Substituting Eq. (2.70) into Eq. (2.67) and applying the parabolic approximation from Eq. (2.71) we get for the first order in χ^2/w^2:

$$\chi^2\frac{d}{dkz}\left[\frac{1}{w}\frac{dw}{dkz}\right] = -\frac{\chi^2}{R^2} + \frac{4\chi^2}{w^4} + \left[-\frac{w_0^2}{w^2}2\frac{\chi^2}{w^2}\mathcal{E}_{r,0}^2 + 3a\frac{w_0^3}{w^3}\frac{\chi^2}{w^2}\mathcal{E}_{r,0}^3\right]. \tag{2.73}$$

Performing the derivation and making use of Eq. (2.70):

$$\frac{d^2w}{dk^2z^2} = -\mathcal{E}_{r,0}^2\frac{w_0^2}{w^3}\left(2-3a\mathcal{E}_{r,0}\frac{w_0}{w}\right) + \frac{4}{w^3}. \tag{2.74}$$

The successive terms on the right hand side can easily be interpreted as a self-focusing term which, because of the normalization, is simply $-w\mathcal{E}_{r,0}^2w_0^2/w^2$ and a

self-defocusing term in $\chi^{(4)}$, and proportional to the cube of the field and the plasma parameter a, and a diffraction term $4/w^3$. The last equation is of the form $d^2y/dz^2 = f(y)$, which can be integrated as $(dy/dz)^2 = 2\int_{y_0}^{y} f(y')dy'$. For the particular case of Eq. (2.74) we have the solution:

$$\left(\frac{dw}{dkz}\right)^2 = \left(2\mathcal{E}_{r,0}^2 w_0^2 - 4\right)\left[\frac{1}{w^2} - \frac{1}{w_0^2}\right] - 2a\mathcal{E}_{r,0}^3 w_0^3\left[\frac{1}{w^3} - \frac{1}{w_0^3}\right] + \frac{w_0^2}{R_0^2}. \tag{2.75}$$

where the last term is the initial value of $(dw/dz)^2$, if $R_0 \neq \infty$.

Including the attachment coefficient γ

Let us first consider the lossless situation ($b = 0$), and insert the Gaussian ansatz:

$$\tilde{\mathcal{E}}_r(kz, \chi) = \frac{w_0}{w(kz)}\mathcal{E}_{r,0} e^{-\chi^2/w(kz)^2} e^{-i\frac{\chi^2}{2R} - i\varphi(kz)} \tag{2.76}$$

where the phase factor on axis $\psi(kz)$, the *normalized* beam size $w(kz)$ and the *normalized* wavefront curvature $R(kz)$ are all quantities linked to each other by Maxwell's equation. With the nonlinear propagation equation (2.64), we no longer have the relation that $\varphi(z) = -\arctan(kz/kz_0)$ where kz_0 is the *normalized* Raleigh range. The relation between these function will result from the substitution of Eq. (2.76) into the propagation equation (2.64), separating real and imaginary parts, and identifying terms of the same order in (χ^2/w^2). In the following we will write w instead of $w(kz)$ and R instead of $R(kz)$ for convenience. We perform the three spatial derivatives on the Gaussian beam (2.76) that will have to be substituted in Eq. (2.55):

$$\begin{aligned}
2i\frac{\partial\tilde{\mathcal{E}}_r}{\partial kz} &= \left[-\frac{1}{w}\frac{dw}{dkz} - i\frac{\chi^2}{2}\frac{d}{dkz}\frac{1}{R} - i\frac{d}{dkz}\varphi(kz) + \frac{2\chi^2}{w^3}\frac{dw}{dkz}\right]\tilde{\mathcal{E}}_r \\
\frac{1}{\chi}\frac{\partial\tilde{\mathcal{E}}_r}{\partial\chi} &= \left(-i\frac{1}{R} - \frac{2}{w^2}\right)\tilde{\mathcal{E}}_r \\
\frac{\partial^2\tilde{\mathcal{E}}_r}{\partial\chi^2} &= \left[\left(-i\frac{1}{R} - \frac{2}{w^2}\right) - \left(\frac{\chi}{R}\right)^2 + i\frac{4\chi^2}{Rw^2} + \frac{4\chi^2}{w^4}\right]\tilde{\mathcal{E}}_r
\end{aligned} \tag{2.77}$$

Substituting into Eq. (2.55) yields the following real and imaginary parts:

$$2\left[\frac{d}{dkz}\varphi(kz)+\frac{\chi^2}{2}\frac{d}{dkz}\frac{1}{R}\right]=-\frac{4}{w^2}-\frac{\chi^2}{R^2}+\frac{4\chi^2}{w^4}+\mathcal{E}_r^2--\left(\sqrt{A^2+B^2\mathcal{E}_r^6}-A\right) \tag{2.78}$$

$$2\left[-\frac{1}{w}\frac{dw}{dkz}+\frac{2\chi^2}{w^3}\frac{dw}{dkz}\right]=\frac{4\chi^2}{Rw^2}-\frac{2}{R} \tag{2.79}$$

Considering a beam on axis ($r=0$) and ignoring both the Kerr effect and the plasma defocusing, we can verify the linear limit of Eq. (2.78) for the linear approximation (taking into account the diffraction equation for a Gaussian beam $w=w_0(1+z^2/z_0^2)^{1/2}$):

$$\frac{d}{dkz}\varphi(z)=-2\frac{1}{w_0^2(1+z^2/z_0^2)}=-\frac{1/z_0}{1+z^2/z_0^2}=-\frac{d}{dz}\arctan\frac{z}{z_0}. \tag{2.80}$$

which is the standard expression for a Gaussian beam. Note that, in the dimensionless units that we chose, $kz_0=w_0^2$.

Looking at the terms in Eq. (2.79) that are of zero and first order in r^2/w^2 we find:

$$\frac{1}{R}=\frac{1}{w}\frac{dw}{dkz} \tag{2.81}$$

We note that this last term simply states the physical relation between the broadening of the beam and the wavefront curvature. Before we separate Eq. (2.78) into zero and first order terms in r^2/w^2 we make the parabolic approximation for the electric field near the beam axis so that:

$$\frac{w_0}{w}\mathcal{E}_{r,0}e^{-\frac{\alpha\chi^2}{w^2}}\approx\frac{w_0}{w}\mathcal{E}_{r,0}\left(1-\alpha\frac{\chi^2}{w^2}\right). \tag{2.82}$$

Since we are going to look at the zero and second order terms in χ^2/w^2, we use a Taylor expansion of the plasma defocusing term in χ^2/w^2. The zero$^{\text{th}}$ order term is:

$$-\frac{\omega_p^2}{n_0^2\omega^2}\bigg|_0=-\sqrt{A^2+B^2\mathcal{E}_{r,0}^6\frac{w_0^6}{w^6}}+A \tag{2.83}$$

The first order of the Taylor expansion in χ^2/w^2 is:

$$\frac{d}{d(\chi^2/w^2)}\left(-\frac{\omega_p^2}{n_0^2\omega^2}\right)\bigg|_0=\frac{3B^2\mathcal{E}_{r,0}^6w_0^6}{w^6\sqrt{A^2+B^2\mathcal{E}_{r,0}^6\frac{w_0^6}{w^6}}} \tag{2.84}$$

Substituting the zero-order term in the real part Eq. (2.78), we find an equation for the phase factor on axis φ, which has not been included in previous numerical solutions. In the case of a steady state solution, the value of $d\varphi/d(kz)$ should be equal to the constant β of Eq. (2.57). The equation for the phase is:

$$\boxed{\frac{d}{dkz}\varphi(kz) = \frac{1}{2}\left[\frac{w_0^2}{w^2}\mathcal{E}_{r,0}^2 - \frac{4}{w^2} - \sqrt{A^2 + B^2\mathcal{E}_{r,0}^6\frac{w_0^6}{w^6}} + A\right].} \tag{2.85}$$

Substituting Eq. (2.81) into Eq. (2.78) and applying the parabolic approximation from Eq. (2.82) we get for the first order in χ^2/w^2:

$$\chi^2\frac{d}{dkz}\left[\frac{1}{w}\frac{dw}{dkz}\right] = -\frac{\chi^2}{R^2} + \frac{4\chi^2}{w^4} - \frac{w_0^2}{w^2}2\frac{\chi^2}{w^2}\mathcal{E}_{r,0}^2 + \frac{3B^2\mathcal{E}_{r,0}^6 w_0^6}{w^6\sqrt{A^2 + B^2\mathcal{E}_{r,0}^6\frac{w_0^6}{w^6}}}\frac{\chi^2}{w^2}. \tag{2.86}$$

Performing the derivation and making use of Eq. (2.81):

$$\boxed{\frac{d^2w}{dk^2z^2} = -2\mathcal{E}_{r,0}^2\frac{w_0^2}{w^3} + \frac{4}{w^3} + \frac{3B^2\mathcal{E}_{r,0}^6 w_0^6}{w^7\sqrt{A^2 + B^2\mathcal{E}_{r,0}^6\frac{w_0^6}{w^6}}}.} \tag{2.87}$$

The first term of the right hand side is the self-focusing term, the second the diffraction term, and the last one a plasma defocusing term.

Recapitulation

The final dimensionless equations to solve are Eqs. (2.87) and (2.85). $\mathcal{E}_{r,0}$ is the amplitude of the field normalized to the characteristic field for self-focusing defined in Eq. (2.38). A defined in Eq. (2.53) is a normalized constant related to the attachment of electrons to oxygen. B defined in Eq. (2.54) is a normalized constant related to the three photon ionization and the recombination. w is the normalized beam size (kw).

If more convenient, it is straightforward to re-write Eq. (2.87) with real dimension variables for w, z and k:

$$\boxed{\frac{d^2w}{dz^2} = -2\mathcal{E}_{r,0}^2\frac{w_0^2}{w^3} + \frac{4}{k^2w^3} + \frac{3B^2\mathcal{E}_{r,0}^6 w_0^6}{w^7\sqrt{A^2 + B^2\mathcal{E}_{r,0}^6\frac{w_0^6}{w^6}}}.} \tag{2.88}$$

2.6 Comparison with an eigenvalue approach

The simulation realized by Sukhinin et al [3] using the eigenvalue approach, finds a stable solution for the steady state. This solution suggest a filament with a waist of 600μm and an power of 4.355×10^8 W. The plot shown on figure 2.10 represent the profile of the filament (in black) obtain from the eigenfunction solution of the equation solved by Sukhinin et al.

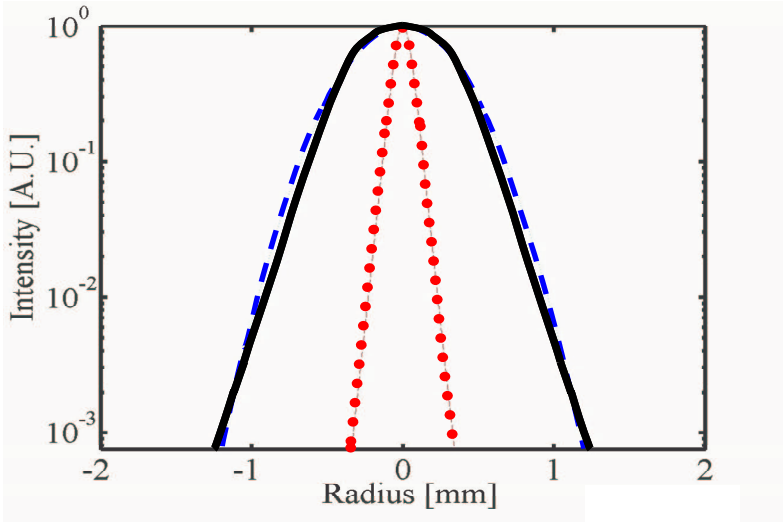

Figure 2.10: Dotted red line: Townes soliton Dashed blue line: Gaussian profile Continuous black line: Eigenfunction solution of the simulation.

We can notice that the simulation shows that the eigenfunction solution of the problem is on the center close to a gaussian profile (blue line) which justify our gaussian approximation in the model. Moreover we can also notice that on the wing, the solution in logarithmic scale has a linear dependance on the radius. This is not the case for the Gaussian but is for a Townes soliton (red line). We can extract for that the filament is neither a Gaussian nor a Townes soliton but a mix of both.

Our propagation simulation on the other hand give a stable solution for a waist of 600μm and a power of 4.982×10^8 W. The two approaches seem to give the same solution to the problem, which confort the accuracy of both approaches. The figure 2.11 shows the propagation of the filament in the steady state conditions. We

can see that the stable solution is obtain because the the filament present nearly no oscillation during it propagation.

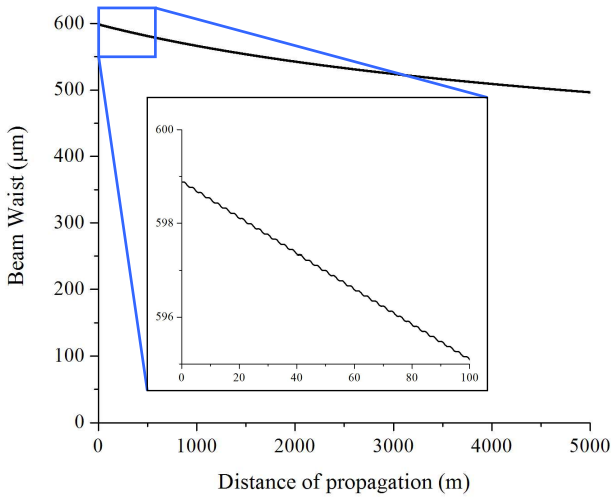

Figure 2.11: Stable solution of the propagation of the filament.

2.7 Simulation Results

As we have seen on figure 2.11 a stable solution for the propagation of the filament in the air is possible. More information can be extracted from the simulation as the power loss during the propagation due to the three photon ionization, but also the phase during the propagation. The figure 2.12 shows those plots. The stable solution is even more confirmed by the linearity of the phase variation during the propagation.

This simulation allows us also to see how the filament will behave if the initial waist is too small (fig 2.13) or if the power is too small (fig 2.14).

We can notice that when we are a little bit out of the optimum conditions for the stable solution the filament present some strong oscillation on its diameter. It can even, if the power is too low after losses, stop the filament propagation (fig. 2.14).

As a conclusion we can see that the two simulations are coherent one with the

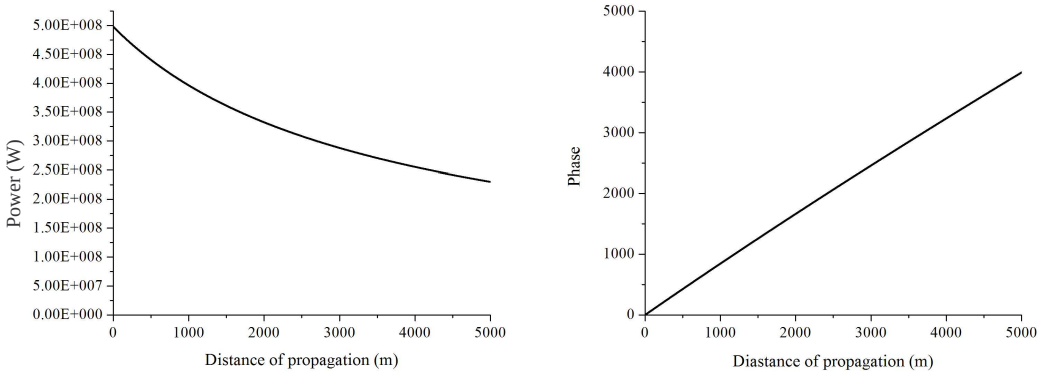

Figure 2.12: Left: Power loss of the filament during propagation due to three photon ionization Right: Phase change of the filament during its propagation.

other and that the filament propagation on very long distance is quite sensitive to the initial conditions.

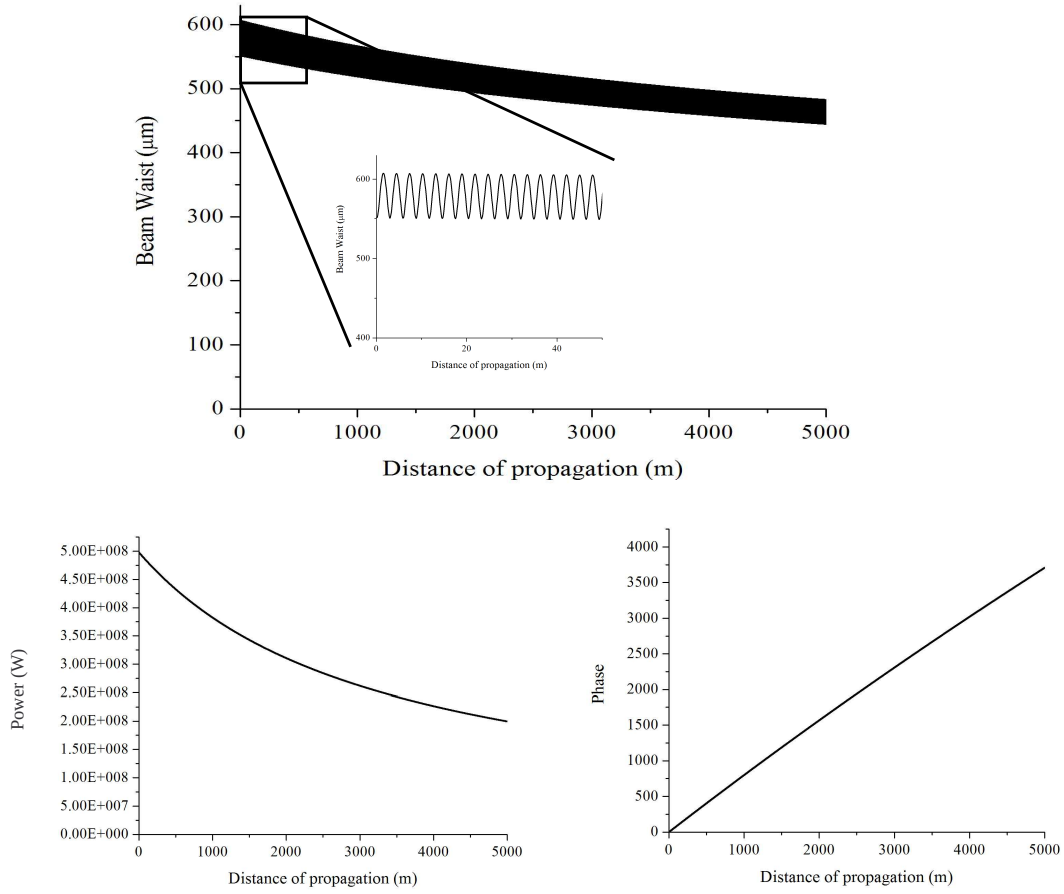

Figure 2.13: Top: Propagation of the filament with a initial waist of 551μm Left: Power loss of the filament during propagation due to three photon ionization Right: Phase change of the filament during its propagation.

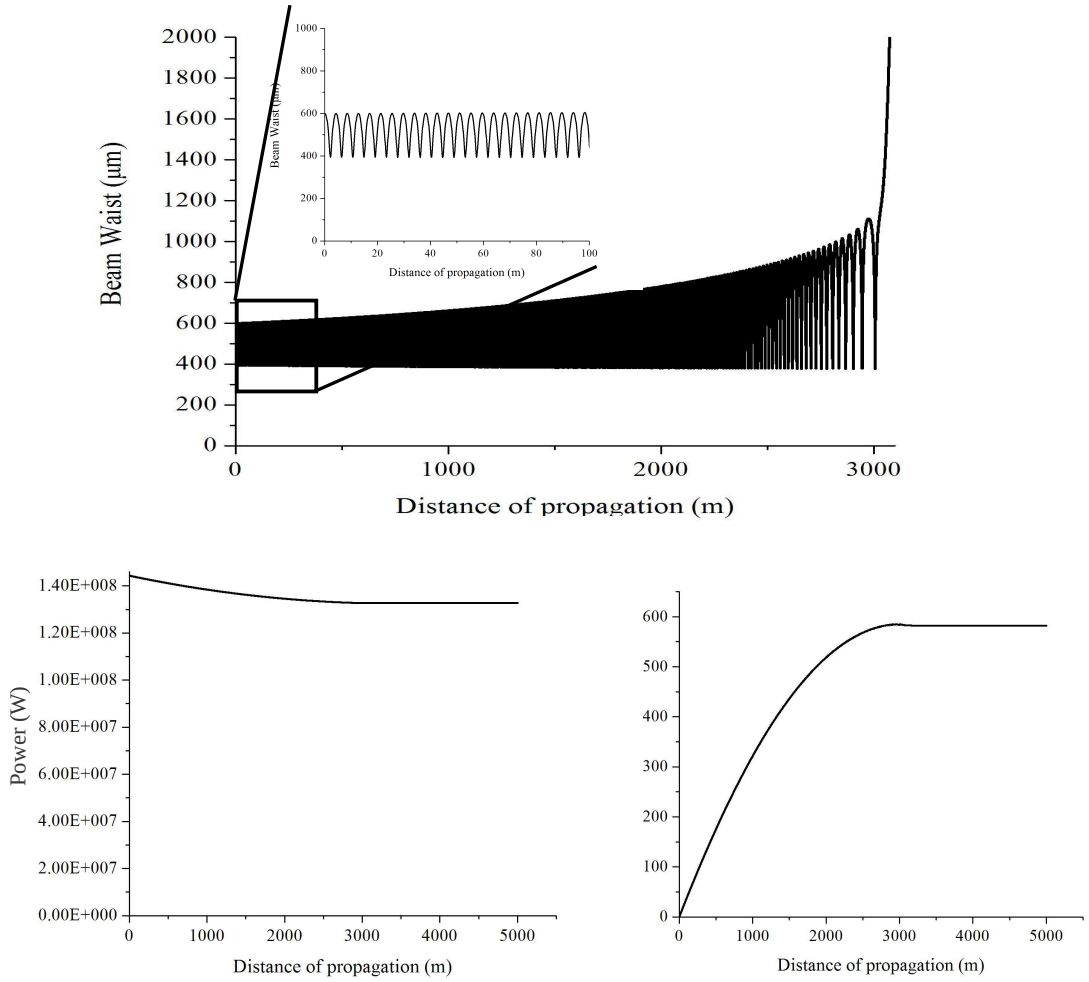

Figure 2.14: Top: Propagation of the filament with a power of 144MW Left: Power loss of the filament during propagation due to three photon ionization Right: Phase change of the filament during its propagation.

Chapter 3

Development of the Laser Source

In this chapter, the experimental Nd:YAG laser will be presented. Each choice of the configuration of the laser will be explained with their advantages and problems and the reasons of those choices. We will start by making a non-exhaustive review of problems encountered during the development of the laser and we will then present the final design of the laser source

3.1 Problem Encountered and Solution

In this paragraph we will explain a few problems that we faced during creating this UV source. Those problems have been solved and we will explain how and what consequence it had on the rest of the system.

3.1.1 Spherical Aberration

The first problem that we faced during the construction of the laser was spherical aberration. In the setup of the laser, three expansions of the laser beam is necessary to pass through each amplifier and optimize the possible amplification. Those increases in size require telescopes which involve three lenses. Those three lenses

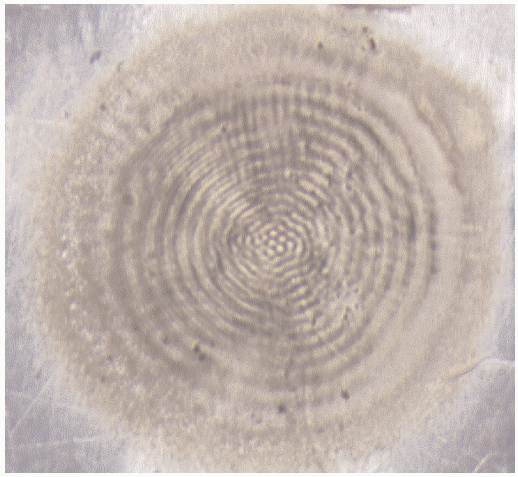

Figure 3.1: Impact of a high power beam at 1064nm on aluminium presenting spherical aberration characteristics.

consist in: two plano-convex lenses made of BK7 with a focal length of +15cm with antireflection coating at 1064nm and a plano-concave lens made of BK7 with a focal length of -5cm with antireflection coating at 1064nm placed between the two positive lens. Adjustments in the distance separating those lenses allow to have a magnification ratio from 0.5 to 2. Those telescopes introduce an spherical aberration, which, in the far-field, introduces a strong modulation of the beam profile. These sharp intensity gradients lead to short scale self-focusing and laser damage in any transparent solid. Figure 3.1 presents the result of the impact of the beam on a piece of aluminium, where the spherical aberration rings are clearly seen. Those rings on a second harmonic crystal tend to, in the best case, reduce the efficiency of the crystal, and in the worst case, at the power level involve, lead to self-focusing and the destruction of the crystal.

To solve this problem all the positive lenses have been replaced by Gradium lenses with antireflection coating at 1064nm. Those lenses present a gradient of index of refraction that corrects for the spherical aberration. The spherical aberration has been strongly reduced using those lenses. Unfortunately lenses with those characteristic and a negative focal length of -5cm are not currently on the market. This prevented us from completely eliminating the problem, but it reduced it to a mangeable level.

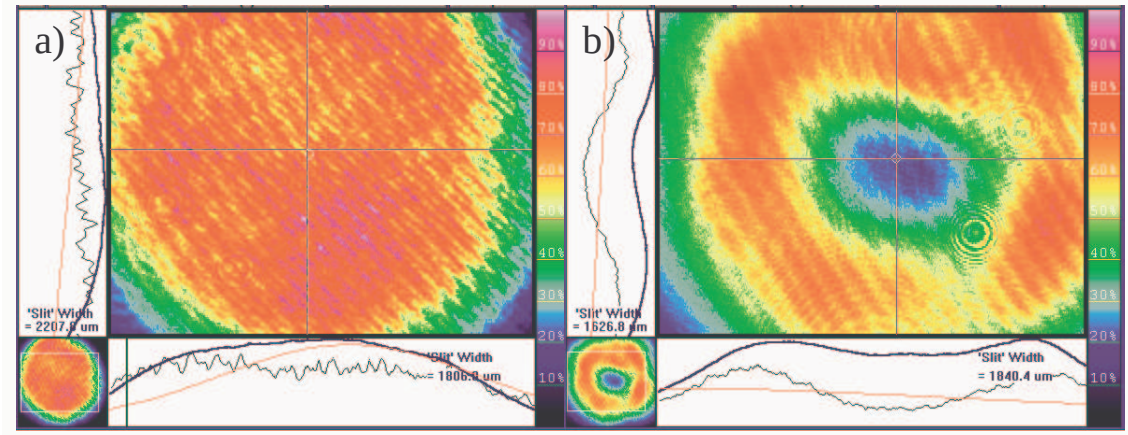

Figure 3.2: Left: beam spatial profile at at the output of the oscillator, Right: Beam spatial profile in the far-field at 3.5meter.

3.1.2 Far-field Spatial Profile of the Beam

Despite the correction of the spherical aberration, the far-field beam profile still shows a ring structure from a different origin. The far-field diffraction pattern is a Bessel function $J_1(r)$. The intermediate pattern is the Fresnel diffraction of a circular aperture, showing the ring structure [13]. Here again, the ring structure lead to short scale self-focusing. The cavity of the laser deliver a flat top beam. This flat top beam in the far-field is transformed in a "donut" shape beam (fig. 3.2). This beam shape causes a lot of problem and in particular the destruction of a 3inches diameter quarter wave plate at 266nm.

To compensate this problem a fundamental change in the oscillator is necessary. The motivations for designing an oscillator with a flat top profile are two fold:

- Extract the maximum amount of power from the oscillator
- Optimize the harmonic generation process.

The first solution to the Fresnel diffraction fringes is to compromise the flat top against a lower order "super Gausssian", by shortening and modifying the cavity. The oscillator consisted initially of a 68cm long unstable cavity with a 5m curvature

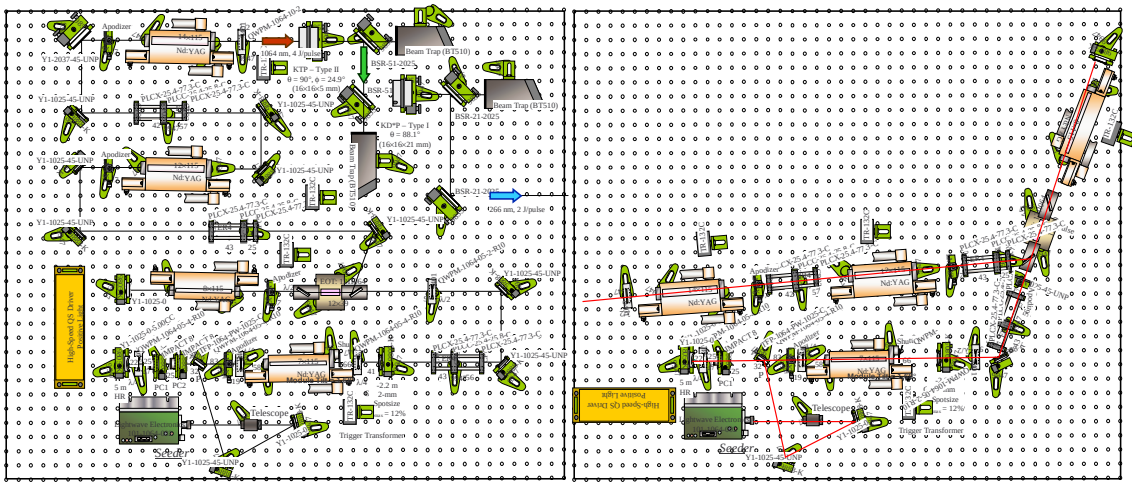

Figure 3.3: Left: Original laser layout, Right: First reduced setup tested.

end mirror. The end mirror was replaced with a 3m curvature end mirror. Moreover to prevent getting into the far field we designed the shortest possible amplifier line without losing too much power. Figure 3.3 present the original setup of the laser and the first reduction in size of the laser amplifier chain before the final disposition of the amplifier was adopted.

Those fundamental changes allowed to prevent the too strong "donut" effect in the first nonlinear effect following the amplifier system. Moreover the following stimulated Brillouin scattering part, due to its phase conjugaison, allowed a compensation of the problem for the rest of the experiment.

Another problem that appeared, was the destruction of rods by focusing reflection from antireflection coated lens inside the rods. The antireflection coating are usually guaranteed for a reflection of less than 0.25%. Unfortunately with a high power beam this is still enough to induce damage. The telescope lenses have been placed in the setup at a sufficiently large distance from the previous rod long enough to prevent any damage in those rods.

Figure 3.4: Self-focusing of the beam after SHG describing a ring according to a super Gaussian profile beam theory.

3.1.3 Self-focusing in Non-linear Crystals

The next improvement was to use the phase conjugated properties of stimulated Brillouin scattering to restore a flat-top beam profile at the nonlinear crystal. To this effect the stimulated Brillouin scattering (SBS) was primarily performed in the infra-red at 1064nm. The reflectivity of the stimulated Brillouin scattering under those conditions was very high (92%). The beam was then sent to a second harmonic crystal which was placed at a distance from the SBS system matching the distance from the oscillator to the SBS system. Because of the phase conjugaison properties of the SBS, the beam at the nonlinear crystal has the same profile as the beam from the oscillator. There are two disadvantages to this approach:

- Pulse compression at 1064nm is not as efficient as at 532nm due to the longer phonon lifetime
- With an energy of 3J and a duration of 600ps, the compressed pulse has a peak power of 5GW, sufficient to create self-focusing in the harmonic generation crystal.

Figure 3.4 presents the self-focusing occurring in the second harmonic crystal. The self-focused spots are distributed on a ring. This pattern of self-focused spots is commonly observed with super Gaussian beam profile, as explained by Fibich [14] Only one solution was possible to solve both problems: generating the second harmonic

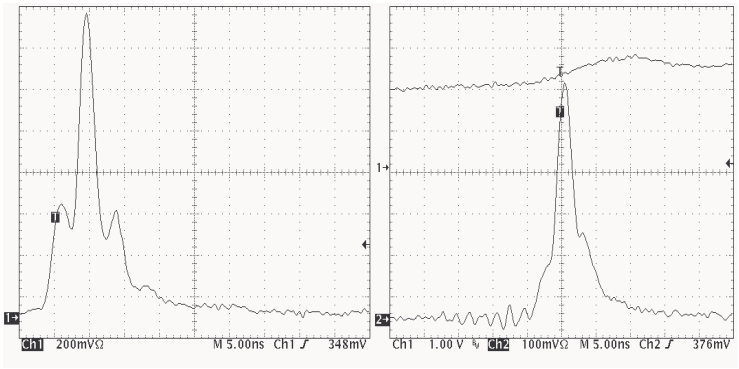

Figure 3.5: Left: Pulse profile with a long cavity presents three pulses right: pulse profile with the short cavity. The side pulses have been eliminated.

before the stimulated Brillouin scattering. As will be seen in Section 3.4 on Brillouin scattering, a Gaussian shaped temporal pulse profile is required for optimum compression. This implies the use of the shortest possible oscillator cavity, resulting in a lower pulse energy, and less efficient generation.

3.1.4 Temporal Profile of the Pulses

The requirements for efficient stimulated Brillouin scattering are not only a sharp spectral bandwidth, but also a smooth rise of the pulse. Unfortunately the original configuration of the cavity with the end mirror and the output coupler separated of 68cm gives a pulse consisting in three sub-pulses. A small pulse precede the main pulse and then another small pulse is following as shown on figure 3.5.

Shortening the cavity allow less longitudinal modes to be present, which implies a diminution of this ringing effect. The cavity was consequently reduced to a 48.5 cm length. The end mirror, originally with a 5m radius of curvature, was replaced with an optimum 4m radius of curvature to stay in the same condition from the stability point of view.

Those changes resulted in the expected conclusion. The side pulses were eliminated as shown on figure 3.5.

All those problems combined brought us to the final design that will be detailed in the following paragraphs.

3.2 Oscillator

The laser is based on a Q-switch Nd:YAG linear oscillator designed as an unstable oscillator. The end mirror has a 4m concave curvature mounted on a piezoelectric translation element. The output-coupler is a 2.2m convex curvature Gaussian mirror with a maximum reflectivity of $R_{max} = 14\%$ and an aperture diameter of 2mm. Those characteristics allow to expect the emission of a beam presenting a super-Gaussian profile (flat top). The output-coupler is placed at 485mm from the end mirror defining the length of the oscillator cavity.

The other elements presented in figure 3.6 inside the cavity will be explained one by one.

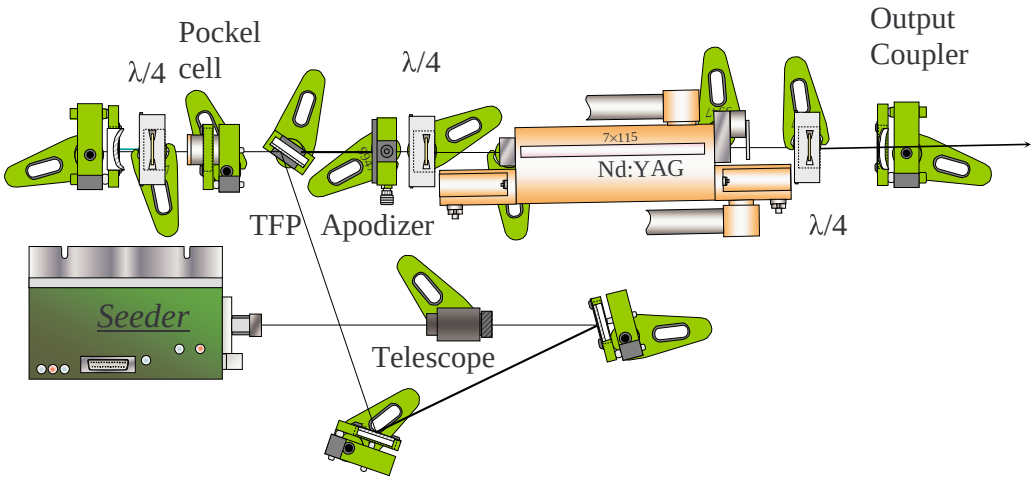

Figure 3.6: Laser oscillator based on Q-switch seeded unstable cavity.

The gain medium is a Nd:YAG rod with parallel faces cut at 2 degree angle. The rod is 115mm long and 7mm diameter. It is orientated such that the translation due to the angled parallel faces produces a displacement only on the horizontal direction. The gain medium is pumped by a single flashlamp at a repetition rate of 2Hz. This

low repetition rate is due to the small efficiency of the completely independent cooling system of the whole laser. The laser head is preceded and followed by 2 quarter wave plates to have a circular polarization inside of the gain medium. Circular polarization prevents spatial hole burning (SHB) a cause of mode hop in the cavity. In a stable linear cavity the gain is saturated at the anti-nodes of the standing wave. This causes instability in the longitudinal modes because the gain for the mode half a wavelength away is higher than the oscillating mode; hence the mode hops. When two quarter wave plates are added (fig. 3.6) the polarization is circular in the rod, so the counter-propagating modes do not create anti-nodes and therefore do not cause SHB. This is called "twisted mode", first presented by Etuhov and Siegman in 1965 [15].

The Q-switching process is realized by a set of a quarter wave plate and a Pockel cell placed in front of the end mirror. The Pockel cell is a 20mm crystal with an 8mm aperture triggered by a 2kV, 2ns rise time electrical pulse generated by a "Positive light" driver. Those elements are preceded by a thin film polarizer that allows to inject a seed laser beam. Q-switching is provided by polarization selection of a thin film polarizer plate and polarization control of a Pockel cell. The polarizer beam splitter sets the horizontal polarization for transmitted light. The vertical polarization of the seeder is switched to horizontal by double pass through the quarter wave plate and propagates through the Nd:YAG. When the Pockel cell is on, the combination of the quarter wave plate and the Pockel cell leads to vertical polarization of the seeder that reflects off the polarizer plate.

Due to the use of stimulated Brillouin scattering in the chain of nonlinear optical processes, it is necessary to seed the oscillator with a sharp bandwidth beam. To adapt the laser cavity length to have the seeded wavelength matching the maximum gain of the laser the end mirror is mounted on a piezo-electric element. When the laser is running a small portion of the laser beam is sent back into the Light Wave Electronics head which compares the wavelength of the laser with the one of the semiconductor reference laser and adjusted the cavity length to have them match. The result of this seeding process is a sharp spectral bandwidth of the emitted light and a reduction of about 15ns of the build up time during the Q-switching (Fig 3.7).

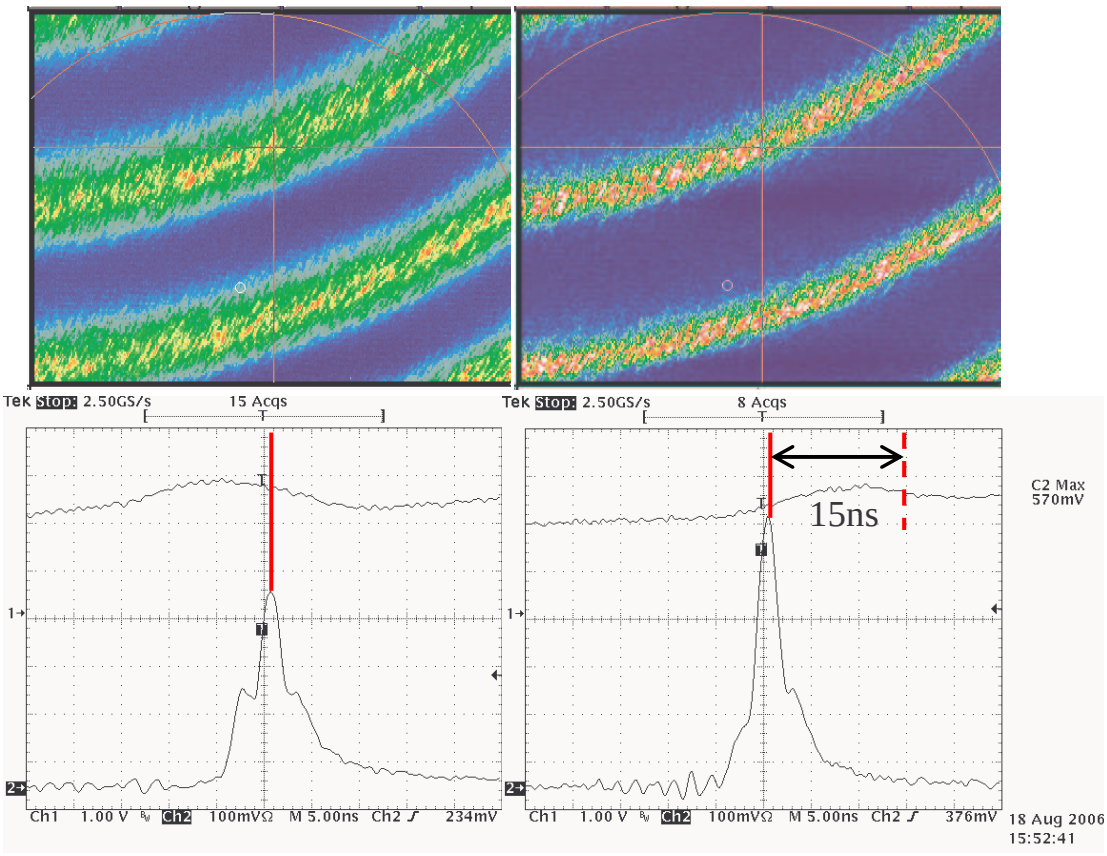

Figure 3.7: Top: Spectral bandwith obtained through a Fabry-Pérot interferometer The free spectral range of the interferometer is 3.4cm^{-1} Left: Oscillator not seeded: large spectrum and long build up time Right: Oscillator seeded: sharp bandwidth spectrum Bottom: Pulse temporal profile with Q-switch trigger signal Left: not seeded Right: seeded: reduction of 15ns of the build up time in comparison of the Q-switch trigger signal.

Finally, inside of the oscillator, an apodizer is placed to clean the beam, and limit its size to prevent clipping on the different optical elements.

The polarization at the polarizing beam splitter is fixed to be horizontal. Going toward the output coupler the beam first meets a quarter wave plate which makes it circularly polarized. Then the beam propagate through the gain medium and finally passes through another quarter wave plate before getting to the output coupler. This makes the output of the cavity being vertically polarized.

The output of the oscillator cavity presents a laser beam vertically polarized with a flat top profile (Fig. 3.8), a pulse duration of 3ns at a repetition rate of 2Hz and

an energy of 200mJ per pulse.

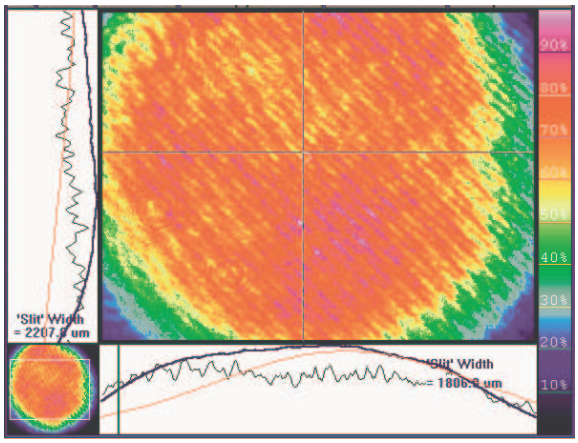

Figure 3.8: Flat top beam profile of the beam at the output of the resonator.

3.3 Amplifier

After the cavity the beam is vertically polarized. A half wave plate placed just after the output coupler brings the polarization to a horizontal configuration. A set of three lenses increases the size of the beam. This set of lenses consist in a converging lens of a focal length of 15 cm followed by a 5cm diverging beam and finally another 15cm converging lens to recollimate the beam. This telescope system allows easy adjustment of the magnification factor from 0.5 to 2. A telescope has been placed before every amplifier as shown in figure 3.9. Moreover this setup avoids any focal point that would create breakdown at those level of power.

When the beam is expanded it passes through an apodizer to have a smooth and well defined beam size at the entrance of the amplifier. The first amplifier is 115mm long and 8mm diameter. The pump power is independently controlled. The beam is then directed into a half wave plate and an isolator with a 12mm clear aperture. The isolator is placed after the first amplifier, unlike the classical position between the oscillator and the first amplifier. This order is chosen to prevent damage to the first amplifier. Due to the stimulated Brillouin scattering nonlinear process there is

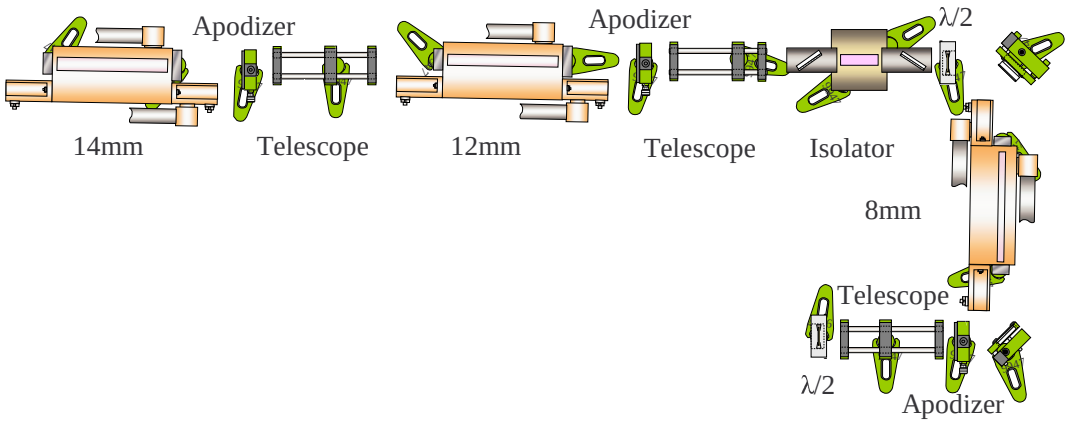

Figure 3.9: Amplifier chain of the laser system.

a leak of a short pulse into the amplifier chain. This small leak, considering gain at each stages, leads to high power pulse that may exceed the damage threshold of the Nd:YAG rod in the first amplifier.

The beam goes to another telescope and apodizer before entering a 12mm diameter amplifier. Another set of telescope and apodizer prepare the beam to enter the last amplifier with a 14mm diameter rod. The second and third amplifier are controlled with coupled drivers. The pump power applied to both amplifiers is the same.

At the end of the amplifier chain the beam still maintains a flat top beam profile (Fig 3.10) with a pulse duration of about 3ns, the energy per pulse having increased to approximately 3J per pulse.

A picture of the oscillator and amplifier chain is presented in figure 3.11.

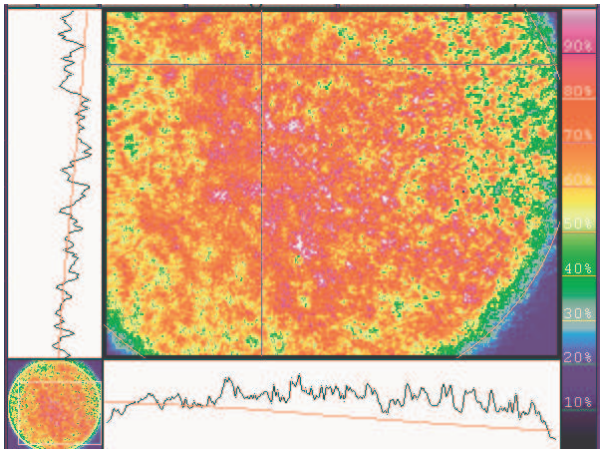

Figure 3.10: Flat top beam profile of the beam at the output of the laser system.

3.4 Pulse Compression: Stimulated Brillouin Scattering

3.4.1 Spontaneous Scattering

Spontaneous emission occurs when light interacts with matter and changes its optical properties. If those properties are not anymore homogeneous, it creates a new

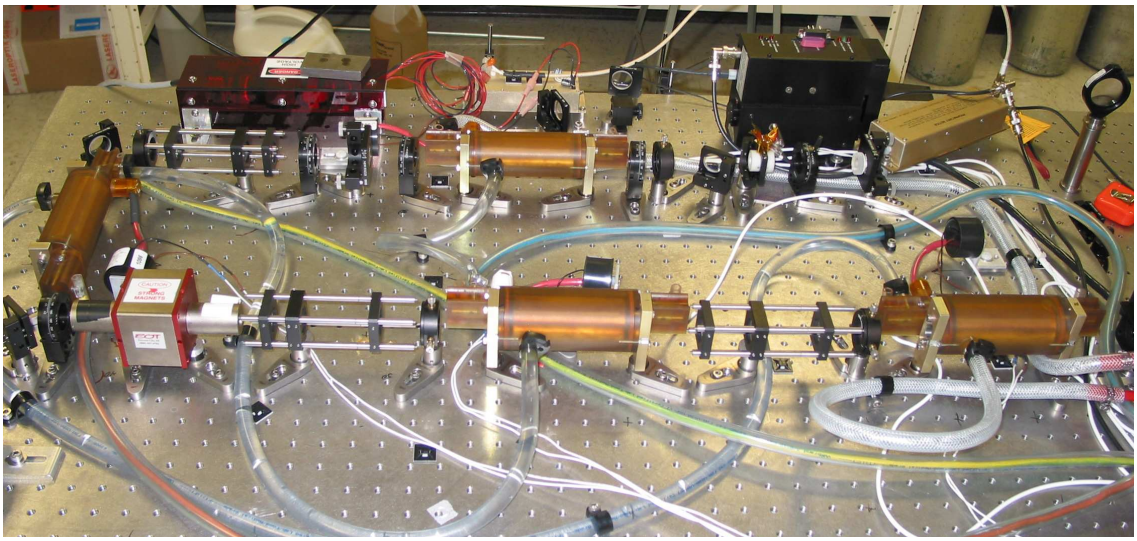

Figure 3.11: Picture of the laser system.

angular and frequency spectrum. Three main phenomenon creating scattering can be outlined, each of them presenting typical properties. Those three scattering are designated as Raman, Brillouin and Rayleigh scattering. They are differentiated by three parameters, which are: the frequency shift Ω_X, the line-width Γ_X, and the scattering cross section σ_X (table 3.1). The spectrum of the scattered light issue from a monochromatic light with the frequency ω_0 submitted to those phenomenon is presented in Fig. 3.12. This spectrum presents six parts which could be define as the Stokes and anti-Stokes Raman, Stokes and anti-Stokes Brillouin, Rayleigh and Rayleigh-wing.

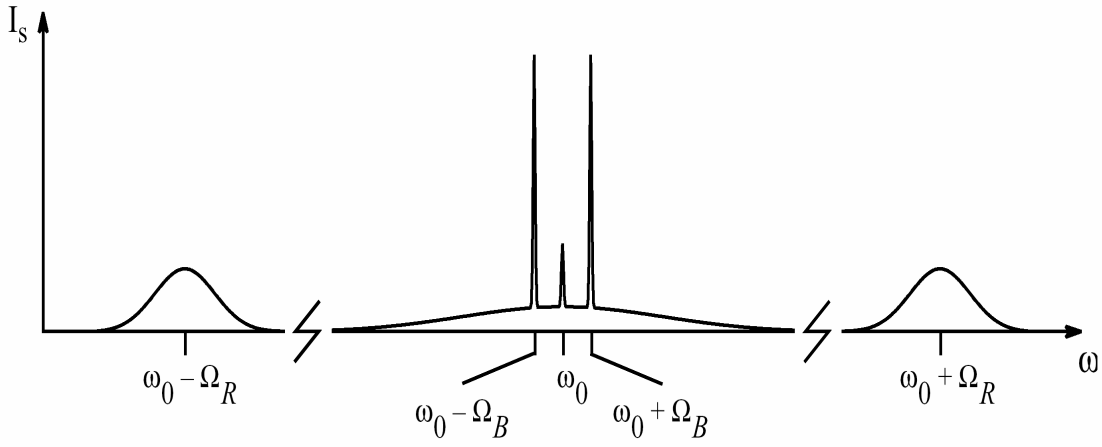

Figure 3.12: Spontaneous light scattering.

The scattering, which presents the largest shift of the order of 1000cm^{-1} is from vibrational modes of the molecules constituting the medium and is known as Raman scattering. In the spectrum shown in Fig. 3.12 we could observe only one pair of Stokes and anti-Stokes for the Raman scattering but in a polyatomic molecular system, or for a crystal with different atoms in the unit cell, there are many such vibrational frequencies, each creating a pair of Stokes ($\omega_0 - \Omega_R$) and anti-Stokes ($\omega_0 + \Omega_R$). At the room temperature the populations of the excited vibrational modes are very low. As a consequence, the anti-Stokes intensities are small in comparison of the associated Stokes components. The line-width of the Raman scattering is typically of the order of a few thousand cm^{-1}, and the lifetime of the excited state

Process	Shift (cm^{-1})	Linewidth (cm^{-1})	Relaxation time (sec)	Gain (cm/MW)
Raman	1000	5	10^{-12}	5×10^{-3}
Brillouin	0.1	5×10^{-3}	10^{-9}	10^{-2}
Rayleigh	0	5×10^{-4}	10^{-8}	10^{-4}
Rayleigh-wing	0	5	10^{-12}	10^{-3}

Table 3.1: Typical values of the parameters describing several light scattering processes.

of the order of a few pico-seconds.

The broad peak centered around ω_0 correspond to the Rayleigh wing scattering from fluctuations in the orientation of anisotropic molecules. Its characteristic time $\tau_{RW} = 4\pi a^3 \eta_s / 3kT_0$ with a the average molecular radius, and η_s the viscosity at room temperature. Its value is of the order of several pico-seconds, while the light extends over many wavenumbers.

The central triplet $(\omega_0, \omega_0 \pm \Omega_b)$ is due to the scattering from the classes of thermally excited fluctuations. The unshifted line at ω_0 is the spontaneous Rayleigh scattering from entropy fluctuations at constant pressure, while the two satellites are the Stokes and anti-Stokes components of the spontaneous Brillouin scattering from adiabatic fluctuations of density propagating with the velocity of sound in the medium.

3.4.2 Stimulated Brillouin Scattering

All those spontaneous emission could be amplified and brought from a spontaneous to a stimulated scattering. The most well known of them being the stimulated Raman scattering (SRS) used in different application to create new frequency due to its large frequency shift. It is even used to identify materials through Raman spectroscopy due to the important knowledge of the typical frequency shift of a lot of materials. The Brillouin scattering is on the other hand a little bit less known but still frequently used through the high power laser community due to its properties of

four wave mixing and phase conjugation mirror that we will develop in this section. We will then discuss another property of the stimulated Brillouin scattering that is more and more investigated which is the pulse compression.

Four-wave Mixing and Phase Conjugation

We will consider two counter propagating plane waves of amplitudes E_1 and E_2 that are the pump beams. A third beam, probe beam, of amplitude E_p interferes with them. The probe beam interfering with one of the pump in the non-linear material creates a dynamic volume hologram by changing its properties. This hologram diffracts the second pump beam according to the Bragg conditions. The grating formed has a wave vector amplitude $k = 2\pi/\Lambda$. The fringe period Λ is given by $\Lambda = \lambda/2\sin\theta$, where λ is the laser wavelength and θ the incident angles between the probe and the pump beam with respect to the normal of the non-linear media. This generates a backward conjugated wavefront for which the complex amplitude can be written: $\mathcal{E}_c = \mathcal{E}_p^* \mathcal{E}_1 \mathcal{E}_2$. As this setup involves simultaneously $\mathcal{E}_1$, $\mathcal{E}_2$, $\mathcal{E}_p$ and $\mathcal{E}_c$ it is called four-wave mixing.

Knowing this we can define a reflectivity for the formed mirror as $R = |\mathcal{E}_c(0)/\mathcal{E}_p(0)|^2$. Considering ω_1, ω_2 and ω_p as the respective frequency of the light for the two pump beams and for the probe beam we can define the frequency of the conjugated beam as $\omega_c = \omega_1 + \omega_2 - \omega_p$. From this general equation we can extract two particular cases: the degenerate four-wave mixing conditions where all frequencies are equal to ω_0, and the quasi-degenerate case where $\omega_c = \omega_0 - \delta$ where $\delta \ll \omega_0$ when the probe and pump frequencies are respectively $\omega_0 + \delta$ and ω_0. This situation is the one encountered during stimulated Brillouin scattering four-wave mixing where the frequency detuning δ is of the order of several gigahertz to a few hertz.

By considering a set of coupled wave equations which describe the space and time evolution of the waves that interact all together in the nonlinear media, Yariv and Pepper [16] first derived the original equations of degenerate (or nearly degenerate) four wave mixing. In the hypothesis of a nondepleted pump beam and equals

frequencies we obtain the following set of coupled equations for the steady state amplitude of the optical fields $\mathcal{E}_c$ and $\mathcal{E}_p$:

$$\frac{d\mathcal{E}_c}{dz} = i\frac{\omega_0}{2}\sqrt{\frac{\mu}{\epsilon}}\chi^{(3)}\mathcal{E}_p^*\mathcal{E}_1\mathcal{E}_2, \tag{3.1}$$

$$\frac{d\mathcal{E}_p}{dz} = -i\frac{\omega_0}{2}\sqrt{\frac{\mu}{\epsilon}}\chi^{(3)}\mathcal{E}_c^*\mathcal{E}_1\mathcal{E}_2, \tag{3.2}$$

where ω_0 is the optical frequency of the beams, $\chi^{(3)}$ is the third-order nonlinearity, and μ and ϵ are the susceptibility and permittivity of the media. By introducing a coupling constant proportional to the pump beam amplitudes $\mathcal{E}_1$ and $\mathcal{E}_2$ and to the third-order nonlinear coefficient of the media $\chi^{(3)}$ we can simplify the equations:

$$\frac{d\mathcal{E}_c}{dz} = -iK^*\mathcal{E}_p^*, \tag{3.3}$$

$$\frac{d\mathcal{E}_p}{dz} = -iK^*\mathcal{E}_c^*, \tag{3.4}$$

where $K^* = i(\omega_0/2)\sqrt{\mu/\epsilon}\chi^{(3)}\mathcal{E}_1\mathcal{E}_2$. Solving these coupled differential equations leads to the expressions for the transmitted and reflected fields for a materials interaction length L:

$$\mathcal{E}_c(0) = -i\mathcal{E}_p^*(0)\frac{K^*}{|K|}\tan|K|L, \tag{3.5}$$

$$\mathcal{E}_p(L) = \mathcal{E}_p(0)\frac{1}{\cos|K|L}, \tag{3.6}$$

Two important parameters could be extracted from those equations of interest for application of degenerate four-wave mixing: first, the reflectivity $R = |\mathcal{E}_c(0)/\mathcal{E}_p(0)|^2$ of the nonlinear phase conjugate mirror, and second, the gain $G = |\mathcal{E}_p(L)/\mathcal{E}_p(0)|^2$, which characterizes probe beam amplification. Those parameters can be expressed as following:

$$R = \tan^2|K|L, \tag{3.7}$$

$$G = \frac{1}{\cos^2|K|L}, \tag{3.8}$$

This shows that amplified reflection and transmission can occur for $|K|L$ satisfying $\pi/4 < |K|L < 3\pi/4$. In these conditions, the nonlinear interaction can be seen as a parametric amplifier for both the reflected and transmitted waves due to efficient energy transfer from the pump beams.

Since amplification appears to be independent from the pump-probe beam angle in the above formula, four-wave mixing could permit to amplify complex incident and conjugate wavefront carrying spatial informations.

Another important configuration for conjugation consists only of an aberrated signal beam that is reflected back by the nonlinear medium in a conjugate wavefront. This particular interaction, called self-pumped phase conjugation, does not require external counter-propagative pump beams, which interfere with signal wave. As a consequence the maximum conjugate beam reflectivity is equal to the unity since there is no gain due to the transfer of energy from a pump beam as it is the case for the classical four-wave mixing geometry. The phase conjugate beam originates from the coherent noise due to the signal beam. It generates in the nonlinear medium complex reflection, types of holographic volume gratings which are due to the interference of the signal with scattered plane waves components that propagate in opposite directions. It results, in regions in the nonlinear medium where there is equivalent of a four-wave mixing interaction, in a self-generated conjugated wave of the incident one. Self pumped conjugation is very well suited in interactions involving stimulated Brillouin scattering. The stimulated Brillouin scattering can like this easily be assimilated to a simplified case of four-wave mixing interaction [17].

Phonon Lifetime Compression

Not only phase conjugation can be achieved by stimulated Brillouin scattering. Another consequence of this interaction in those nonlinear media can be compression of the conjugated pulse. In particular conditions, the stimulated Brillouin scattering can be the dominant process of laser-matter interaction. To be able to describe this process both the field and the medium have to be treated in the same time and

in a correlated manner [18]. To do so, we use the Navier-Stokes and the Maxwell equations. We will consider an acoustic and thermal scattering waves and neglect other nonlinear phenomena. The slowly varying amplitude approximation leads to coupled equations for the envelopes of pump and scattered electromagnetic waves $\mathcal{E}_p$ and $\mathcal{E}_S$ with amplitudes of scattering density and temperature waves ρ and T:

$$
\begin{aligned}
-\frac{\partial \mathcal{E}_S}{\partial z} + \frac{n}{c}\frac{\partial \mathcal{E}_S}{\partial t} + \frac{\alpha}{2}\mathcal{E}_S &= \frac{\imath\omega_S}{4cn}[\frac{\gamma^e}{\rho_0}\mathcal{E}_p\rho^* + (\frac{\partial \varepsilon}{\partial T})_\rho \mathcal{E}_p T^*] \\
\frac{\partial \mathcal{E}_p}{\partial z} + \frac{n}{c}\frac{\partial \mathcal{E}_p}{\partial t} + \frac{\alpha}{2}\mathcal{E}_p &= \frac{\imath\omega_P}{4cn}[\frac{\gamma^e}{\rho_0}\mathcal{E}_S\rho^* + (\frac{\partial \varepsilon}{\partial T})_\rho \mathcal{E}_S T^*] \\
\frac{\partial^2 \rho}{\partial t^2} - (2\imath\omega - \Gamma_B)\frac{\partial \rho}{\partial t} - (\omega^2 - \imath\omega\Gamma_B - \frac{v^2k^2}{\gamma})\rho - 2\imath k\frac{v^2}{\gamma}\frac{\partial \rho}{\partial z} + \frac{v^2\beta_T\rho_0 k^2}{\gamma}T &= \frac{\gamma^e k^2}{8\pi}\mathcal{E}_p\mathcal{E}_S^* \\
\frac{\partial T}{\partial t} - (\imath\omega - \frac{1}{2}\gamma\Gamma_{Rl})T - \frac{\gamma - 1}{\beta_T\rho_0}(\frac{\partial \rho}{\partial t} - \imath\omega\rho) &= \frac{1}{4\pi C_v\rho_0}\mathcal{E}_p\mathcal{E}_S^*[nc\alpha - \frac{\imath\omega T_0}{2}(\frac{\partial \varepsilon}{\partial T})_\rho]
\end{aligned}
\tag{3.9}
$$

where ω, ω_P, ω_S, are acoustic, pump, and stokes wave frequencies. $\Gamma_B = nk^2/\rho_0$ and $\Gamma_{Rl} = 2\lambda_T k^2/\rho_0 C_P$ are Brillouin and Rayleigh linewidths, $\gamma^e = \rho_0(\partial\varepsilon/\partial\rho)_T$ is an electrostriction coupling coefficient, v is a sound velocity, $\gamma = C_P/C_v$ is a ratio of specific heats at constant pressure and constant volume, α is the linear absorption coefficient, β_T is the coefficient of thermal expansion.

The coupled equations represents an ideal, unperturbed SBS interaction. However, this is difficult to satisfy in usual SBS materials at elevated laser intensity.

We will now discuss the stimulated Brillouin scattering, which occurs when the optical field drives acoustic waves in the medium. The general scheme for observing SBS involves a laser field with frequency ω_L which interacts with a co-propagating pressure wave of frequency Ω (Fig. 3.13). The light, which is scattered backwards, according to the energy conservation is down-shifted and its frequency is $\omega_S = \omega_L - \Omega$. The interference between the incident and the scattered optical fields contains an acoustic frequency term at $\Omega = \omega_L - \omega_S$, which, if powerful, enough can itself create an acoustic wave. The resulting amplified acoustic wave can scatter more efficiently the incident field, thus amplifying the scattered light at Stokes frequency (ω_S). This interaction can lead to an exponential growth of the Stokes intensity if both the pump and the Stokes waves overlap over an extended propagation distance. In

focused geometry this is the case of backward scattering only; in forward direction the acoustic wave frequency vanishes. A sharp spectral bandwith of the pump is necessary in order to enhance the interference, which will optimise the reflectivity of the holographic grating formed.

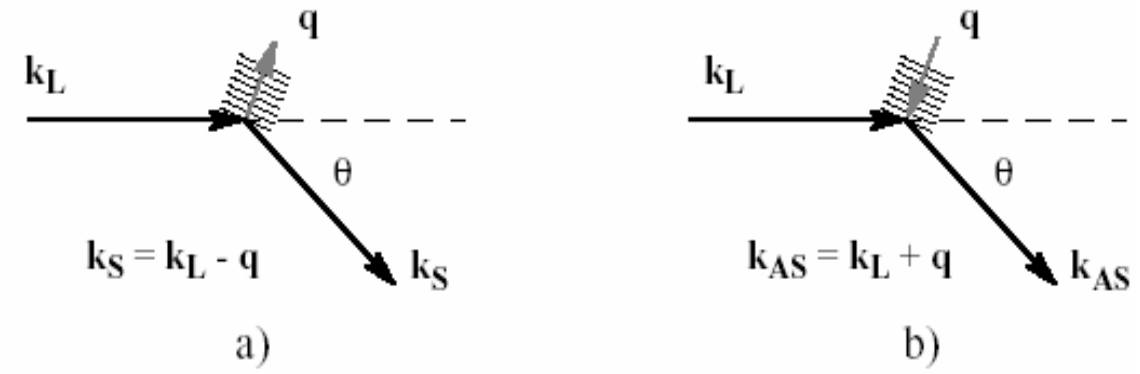

Figure 3.13: Stimulated Brillouin scattering a) Stokes component - b) anti-Stokes component.

The physical mechanism by which the two optical fields can generate a pressure wave is either electrostriction or absorption. The former is always present and is dominant in lossless media, which makes it the most interesting from a practical point of view. The latter occurs in lossy substances only and we shall not discuss it here. The electrostrictively induced pressure, created by a static electric field is given by:

$$p_{st} = -\rho \frac{\partial \epsilon}{\partial \rho} \frac{E^2}{8\pi} = -\gamma_e \frac{E^2}{8\pi}, \tag{3.10}$$

where γ_e is the electrostrictive constant and E is the static electric field strength. The minus sign in the previous equation reflects the fact that the pressure is reduced in regions of high field strength, hence the fluid is drawn into these regions and the density ρ is increasing.

Initiated from backward spontaneous Brillouin scattering the stimulated process involves interaction of three waves: two optical (laser and Stokes) and one acoustic.

We considers them as scalar plane-wave in the form:

$$E_1(z,t) = \mathcal{E}_1(z,t)e^{i(k_1 z-\omega_1 t)} + c.c., \tag{3.11}$$

$$E_2(z,t) = \mathcal{E}_2(z,t)e^{i(k_2 z-\omega_2 t)} + c.c., \tag{3.12}$$

$$\bar{\rho}(z,t) = \rho_0 + \rho(z,t)e^{i(q_B z-\Omega_B t)} + c.c., \tag{3.13}$$

propagating along the z-axis. In the previous equations the frequencies and the wave-vectors satisfy energy ($\omega_1 = \omega_2 + \Omega_B$) and momentum ($k_1 = q_B - k_2$) conservation laws. Under the assumption of small Stokes shift ($\omega = \omega_1 \approx \omega_2$) the acoustic frequency is given for backscattering by: $\Omega_B = 2n\omega v/c$. The two optical fields are governed by Maxwell's equations, whereas the acoustic field is described by the Navier-Stokes equation with electrostrictive driving term:

$$\frac{\partial^2 E_i}{\partial z^2} - \frac{n^2}{c^2}\frac{\partial^2 E_i}{\partial t^2} = \frac{4\pi}{c^2}\frac{\partial^2 P_i}{\partial t^2}, i = 1,2 \tag{3.14}$$

$$\frac{\partial^2 \bar{\rho}}{\partial t^2} - \Gamma\nabla^2(\frac{\partial \bar{\rho}}{\partial t}) - v^2\nabla^2\bar{\rho} = \nabla\cdot\mathbf{f}, \tag{3.15}$$

where $\mathbf{f}$ is the force per unit of volume, defined by $\mathbf{f} = -\nabla\mathbf{p_{st}}$. Substituting Eq.(3.8) into the right-hand side of Eq.(3.13) and taking into account the total optical field is $E(z,t) = E_1(z,t) + E_2(z,t)$ we obtain an equation for the acoustic field:

$$\frac{\partial^2\rho}{\partial t^2} + (\Gamma_B - i2\Omega_B)\frac{\partial\rho}{\partial t} - i\Gamma_B\Omega_B\rho = \frac{\gamma_e q_B^2}{4\pi}\mathcal{E}_1\mathcal{E}_2^*. \tag{3.16}$$

In Eq.(3.12) the polarization due to the density change $\Delta\bar{\rho} = \bar{\rho} - \rho_0$ is $P = \Delta\chi E = \frac{\Delta\varepsilon}{4\pi}E = \frac{\gamma_e}{4\pi\rho_0}\Delta\bar{\rho}E$. Then under slowly varying amplitude approximation and taking into account the phase-matched terms in the polarization

$$P_1(k_1,\omega_1) = \rho\mathcal{E}_2 e^{i(k_1 z-\omega_1 t)} + c.c., \tag{3.17}$$

$$P_2(-k_2,\omega_2) = \rho^*\mathcal{E}_1 e^{i(k_2 z-\omega_2 t)} + c.c.. \tag{3.18}$$

The Maxwell's equations for the optical fields are:

$$\frac{n}{c}\frac{\partial\mathcal{E}_1}{\partial t} + \frac{\partial\ \mathcal{E}_1}{\partial z} = i\frac{\gamma_e\omega}{2nc\rho_0}\rho\mathcal{E}_2, \tag{3.19}$$

$$\frac{n}{c}\frac{\partial\mathcal{E}_2}{\partial t} + \frac{\partial\ \mathcal{E}_2}{\partial z} = i\frac{\gamma_e\omega}{2nc\rho_0}\rho^*\mathcal{E}_1. \tag{3.20}$$

Together Eq.(3.14) and Eq(3.17-18) constitute the set of equations describing the electrostrictive SBS process. This set of three coupled non-linear partial differential equations is difficult to solve in analytical form but certain approximations could be made to find a solution to a steady-state case.

3.4.3 Experiment

The experimental part of the stimulated Brillouin scattering as been a difficult and long part of the project but a configuration has finally been chosen. We are going to explain it in details in the following paragraphs.

Setup

To realize the stimulated Brillouin scattering you first need to chose the medium in which the phenomenon is going to take place. Several parameters have to be taken into account to make the right choice. There is first the kind of medium you want: gas, liquid or solid. For our case solids are immediately eliminated due to the high power we want to achieve. The solid would be destroyed after the first shot. Then we eliminated the gases because they need to be kept at high pressure and they are quite dangerous materials to handle. The safety of our laboratories didn't allow us to use such media. So the liquid are imposing themselves due to their easy manipulation and very high damage threshold.

After this choice come the choice of which liquid to use among all the one possibles. The different values that should be look at for SBS phenomenon application are the Brillouin gain g_B, the phonon lifetime τ_B and the Brillouin shift $\Delta\nu_B$. Those values are presented in the table 3.2 for a few liquids. The conditions for the SBS realized in the laboratory are the following: wavelength λ=532nm, energy per pulse >2J and compression from 3ns to ∼200ps. The choice came to use a fluorinert liquid. Table 3.3 resumes the characteristics for the fluorinerts [19].

The compression was first planned to be realized in water at 266nm, due to the

Liquid	T (^{o}C)	g_B (cm/MW$\times 10^{-3}$)	τ_B (ns)	$\Delta\nu_B$ (cm^{-1})
CS2	20	68	6.4	0.127
Water	20	3.8	1.87	0.125
Acetone	20	15.8	2.67	0.102
CCl_4	20	3.8	0.6	0.96
Fluorinert FC-75	20	4.5-5	0.9	0.45
Fluorinert FC-72	20	6-6.5	1.2	0.41

Table 3.2: The data are presented for a wavelength of 1064nm [19].

phonon lifetime of this liquid. The first medium considered was water. To prevent a strong effect of the fluctuation of the index of refraction of the water function of the temperature the Brillouin cell was continuously cooled at about 4^{o}C where $\frac{dn}{dT}|_{4^oC} = 0$ and filtered to prevent breakdown. Unfortunately after reading different papers from Fry and Pope and Quickenden [20, 21, 22, 23], we discovered that water is transparent at 266nm only in very well purified environment and for a time of only about 20 minutes. All those conditions could not be achieved in our laboratory. So

Fluorinert Property	FC-72	FC-75
Main component	C_6F_{14}	C_8F_{18}
Average molecular weight	340	420
Density (kg/m^3)	1.68	1.77
Boiling point (^{o}C)	56	102
Pour point (^{o}C)	-90	-88
Critical temperature (^{o}C)	178	227
Critical pressure ($\times 10^6$Pa)	1.83	1.60
Specific heat (J/kg K)	1046	1046
Thermal conductivity (W/m K)	0.057	0.063
Expansion coefficient (10^3/K)	1.6	1.4
Viscosity (centistokes)	0.4	0.8
Sound velocity (m/s)	512	563
Dielectric strength (MV/m)	14.9	15.7
Refractive index	1.251	1.276
Optical breakdown threshold (GW/cm^2)	100-130	100-130
SBS threshold E(mJ)	2.5	3.4

Table 3.3: Physical properties of fluorinert liquids [19].

the water was eliminated from our potential SBS medium list.

This option ruled out the choice then went to FC-75 at 266nm due to its compatible phonon lifetime and very high optical breakdown. Based on a paper by Kuwahara et al [24] which was using the fluorinert FC-72 as SBS medium the compression in the UV was possible. We decided to use FC-75 due to its more convenient phonon lifetime for our experiment at 266nm, and its cheaper price. Even after filtering very importantly the medium with a 25nm pore size filters the SBS efficiency was more and more decreasing and some carbon deposit was observed as residu in the filters. An investigation from our side of the lifetime of the fluorinert media for SBS was conducted. The FC-72 is composed of C_6F_{14} while the FC-75 is composed of C_8F_{18} and a small amount of $C_8F_{16}O$ [18] with C-F bonding energy of 5.56eV [25]. Results presented here indicate a limitation on their endurance to the UV. Transmission spectra of both FC-72 and FC-75 show them to be highly transparent from 1100nm to 250nm [26, 27]. At shorter wavelengths there is a sharp increase of absorption.

We have found that the exposure of fluorocarbon liquids (FC-72 and FC-75) to an intense laser radiation can greatly affect their absorption spectrum. A 10cm long 2cm diameter quartz cell, filled with FC-72 (FC-75), is exposed to a laser beam for one hour at a repetition rate of 2Hz. The pulse duration is 3ns and the collimated beam has a diameter of 12mm. The irradiation conditions are summarized in table 3.4. The absorption spectrum was taken before and after the exposure of the liquid to the laser beam. The liquid was changed after each test. The FC-72 and FC-75 were not affected by the experiment at 1064nm. Likewise the FC-72 was not affected by the experiment at 532nm. The FC-75, however, presents absorption proportional to the beam power in the wavelength region of 300 to 350nm while exposed to the 532nm laser beam. The most significant results are when the fluorocarbons are exposed to the 266nm wavelength. The overall transmission is decreased for both liquids proportionally to the power applied. As indicated in figure 3.14 the FC-75 and FC-72 become nearly opaque to the UV beam. We can conclude, from these results, that the UV absorption results in a decomposition of the C-F molecules into carbon particles which in turn leads to a further attenuation of the beam. Knowing that the

λ (nm)	Energy (mJ)	Power (MW)	Intensity (MW/cm^2)
1064	150	50	44
	300	100	88
532	150	50	44
	300	100	88
266	150	50	44
	200	66	58

Table 3.4: Wavelength and energy of laser beam

bonding energy of the C-F is 5.56eV, the observed phenomenon is indicative of a 2 photon dissociation process (4.66eV/photon at 266nm).

We compare next our UV irradiation experiment with the exposure condition

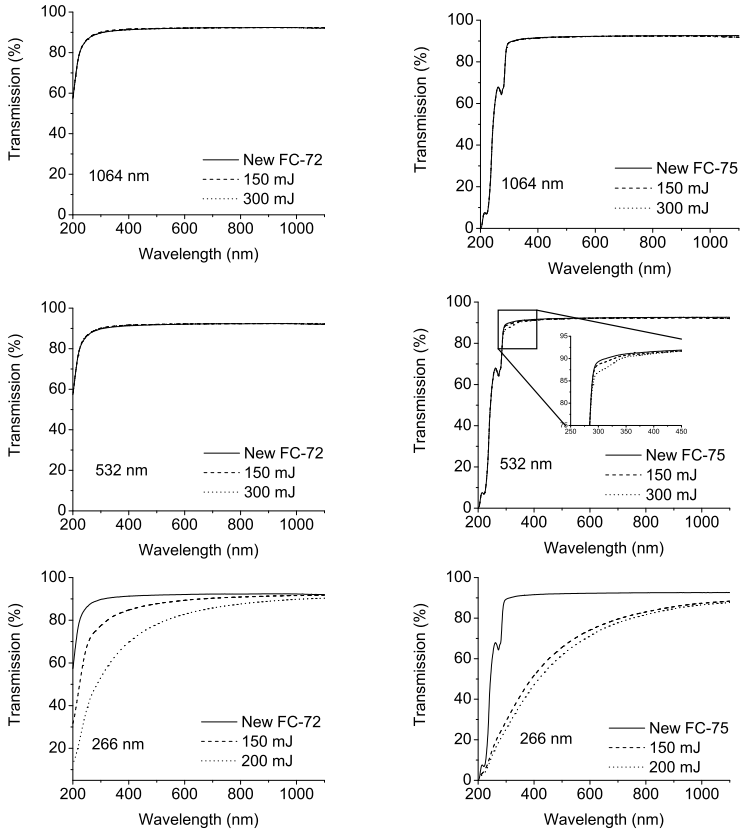

Figure 3.14: Transmission spectrum of FC-72 and FC-75 before and after exposure to 1064nm, 532nm, 266nm for one hour at 2Hz. Each measurement had been performed with two laser powers.

of Kuwahara et al. [24]. They suggested the use of FC-72 for pulse compression of a 248nm laser. The beam diameter reported is 1cm, the energy per pulse is 5.5mJ and the pulse duration 350ps at the entrance to the stimulated Brillouin scattering (SBS) cell. The peak power of 16MW corresponds to an intensity of 20MW/cm^2 for a collimated beam. In their experiment the beam is focused by a 60cm lens into a 15cm SBS cell. This brings the question of the practicality of the technique proposed by Kuwahara et al. [24]. Their intensity at the input of their cell is only a factor 2.2 smaller than the intensity in the UV of our collimated beam. As their beam is focused through a 60cm lens the intensity reached should exceed by several order of magnitude the intensity of our collimated beam. Moreover, their experiment is performed at 248nm, which corresponds to 5.0eV/photon against a photon energy of 4.66eV/photon at 266nm in our experiment. Therefore, it is reasonable to assume that the decomposition that we have observed should also occur during their experiment. The efficiency of the compression phase conjugated mirror created under these conditions should last only for a few pulses ($\sim$ 1000).

After this investigation we decided to make the stimulated Brillouin scattering compression in the infra-red at 1064nm in FC-75. This experiment brought the self-focusing in the second harmonic crystal problem previously explained and the compressed pulse was not compressed enough for our experiment ($\sim$600ps). The phonon lifetime of FC-75 at 1064nm being $\sim$1ns we were hoping to achieve sub-phonon lifetime compression as explained by Veltchev [28]. The complication of the subphonon lifetime compression and the self-focusing problem in the second harmonic generation explained earlier, brought us to change the setup once more.

We then fall back on FC-72 at 532nm. Its phonon lifetime is 295ps which is suited for our experiment.

A tube of pyrex of 10cm diameter and 80cm long is used as SBS cell. The end windows is made of calcium fluoride. The entrance window is made of fused silica and treated for anti-reflection on the air-glass surface. The windows are sealed to the tube by a combination of polypropylene O-rings and Teflon rings hold by an aluminium mount. The tube as been modified to allows circulation of the liquid.

The cell is clean with toluene, acetone and methanol and dried with pressurized nitrogen before filling. The cell needs to be extremely clean to prevent any particles in the liquid which would produce breakdown in the liquid. The liquid before being introduce in the cell passes through a filtration system with a pore size of 25nm. When the cell is filled the filtration system composed of 2 parallel filters with pore size of 25nm circulates constantly except during experiment.

The SBS cell is now built and kept cleaned. This will be used in the single cell configuration for SBS compression. This implies that a lens is placed before the entrance of the cell with a focal length that is equivalent of half the length of the pulse to allow a perfect overlap of the Stokes pulse with the pump pulse into the SBS medium. To make the selection between the pump and the compressed pulses the polarization is used. The pump pulse passes through a thin-film polarizer and a quarter wave plate before the focusing lens, so the polarization at the entrance of the cell is circular. The reflected beam then pass again through the quarter wave plate is then rejected by the thin-film polarizer (fig. 3.15). This is possible because unlike the backward stimulated Raman scattering the stimulated Brillouin scattering do not conserve the angular momentum of the beam.

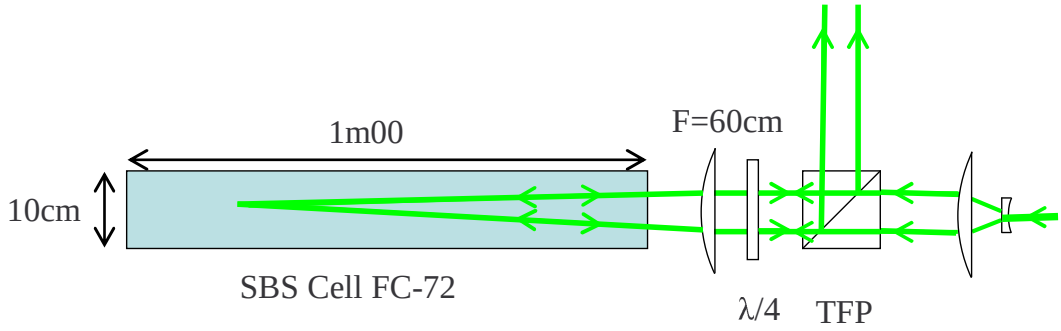

Figure 3.15: Schematic of the stimulated Brillouin scattering setup.

Due to the high initial power of the laser and even higher Stokes power the beam as to present a rather large aperture to prevent damages and have an optimum SBS conversion. This obliged us to have a 10cm diameter thin-film polarizer and a 7cm diameter quarter wave plate. The beam has a diameter D=3.5cm. The diameter is

chosen to satisfy a good ratio f/D to have an optimum conversion [29]. Moreover computer simulation give an optimum result for this configuration (fig 3.16). The choice of the focal length f was made to be 60cm, which allows as expected a good overlap of the pulse inside of the SBS medium.

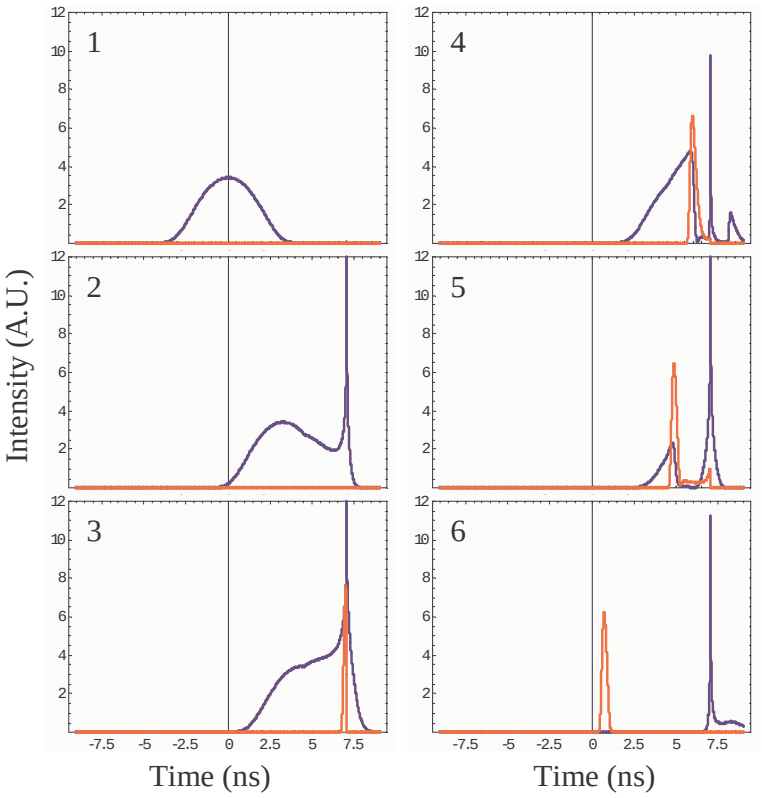

Figure 3.16: Simulation of the SBS compression in FC-72 at 532nm (Pump beam in blue, Stokes beam in Red).

The beam is moreover slightly defocusing before arriving to the system such that due to the phase conjugaison of the SBS phenomenon the reflected beam present a slight convergence. The beam could like this focused after 5.6m of propagation after the SBS system.

Results

First of all the phase conjugation is verified. The beam is converging after the stimulated Brillouin scattering as it is time reverse from the diverging beam. If the

phase conjugation was not satisfied the beam will still be diverging.

The reflection efficiency of the the stimulated Brillouin scattering mirror is quite stable over the range of power that we are using for the experiment (500mJ-2J at 532nm). The SBS phenomenon threshold being rather low for the FC-72 the reflectivity for pump pulse of 3mJ is of about 10% then quickly rises to 65% at 5mJ and then joins a stable value of 80% over 20mJ. This reflectivity considers the full SBS system. It means that it considers the losses in order from the thin film polarizer, the quarter wave plate, the SBS cell window, the SBS reflectivity itself, and then again the cell window, the quarter wave plate and finally the thin film polarizer.

The Stokes pulse is then sent to a Fabry-Pérot interferometer to observe the spectrum. The mirrors for the interferometer at 532nm have a reflectivity of 88% and are separated by 60mm. A 35cm lens placed after the Fabry-Pérot builds in its focal plane the fringes presented on figure 3.17. We can see that on the right the spectrum from the Stokes beam is larger and slightly shifted in frequency in comparison to the spectrum when the beam is reflected from a classical mirror on the left. The frequency shift is expected form the stimulated Brillouin scattering and

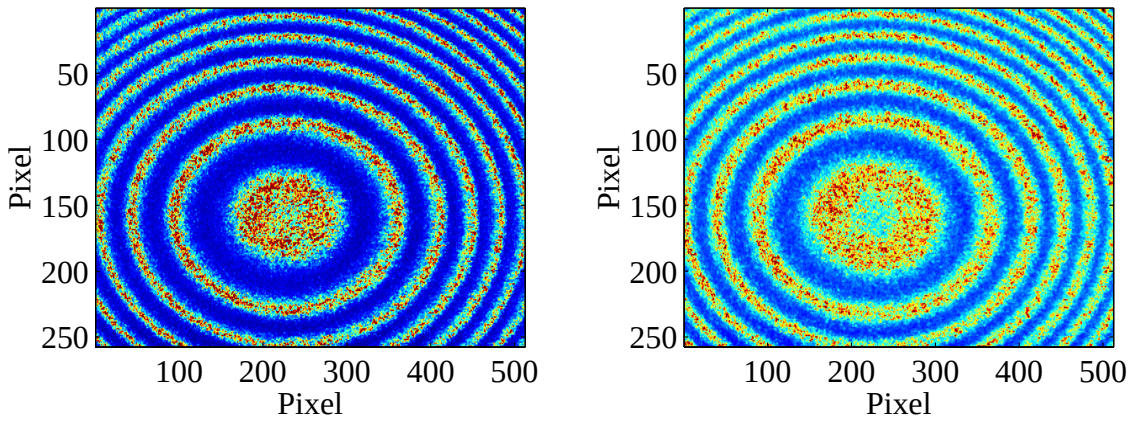

Figure 3.17: Left: interferogram from the Fabry-Pérot of the beam when the SBS cell is replaced by a classical mirror. Right:interferogram from the Fabry-Pérot of the Stokes beam.

correspond to the Brillouin shift of the medium. The broadening of the spectrum is

also expected and is a good sign for the presence of compression of the laser pulse.

The pulse compression is moreover verified by another phenomenon. Two beams with the same energy and same convergence are send to the same second harmonic generator. One of them is issued from the stimulated Brillouin scattering system the other one is obtained with a classical mirror. After optimization of the alignement of the second harmonic generator for both beams, we achieved a conversion efficiency about ten times higher for the Stokes beam than for the pump beam. This is a clear proof that we obtain through stimulated Brillouin scattering a compression of about a factor ten. Starting with a pump pulse of 3ns we can estimate that our Stokes pulse has a pulse duration of about 300ps. This pulse duration would correspond as predicted to the phonon lifetime of the FC-72 at 532nm which is 295ps.

As a conclusion, the stimulated Brillouin scattering delivers us a phase conjugated beam with a pulse duration of 300ps and a mirror efficiency of about 80%. The compression was realized with an initial pulse duartion of 3ns which is approximately five times smaller then anything in the literature at this laser energy [25, 19, 30].

3.5 Harmonic Generation

Before getting from the amplification stage to the nonlinear processes, the beam passes through a half wave plate to have a polarization matching the optimum polarization for the following type II second harmonic generator.

The second harmonic generator crystal is a 14mm×14mm×4mm KTP type II. The second harmonic wavelength is separated from the fundamental through two 2inches dichroic mirrors. The conversion efficiency obtained from the collimated fundamental beam is over 70% (fig. 3.18).

The 532nm beam expanded to a 3.5cm diameter for the stimulated Brillouin scattering. A beam this size is necessary both for optimum SBS compression and also for preventing damage on the optics after compression by decreasing the intensity.

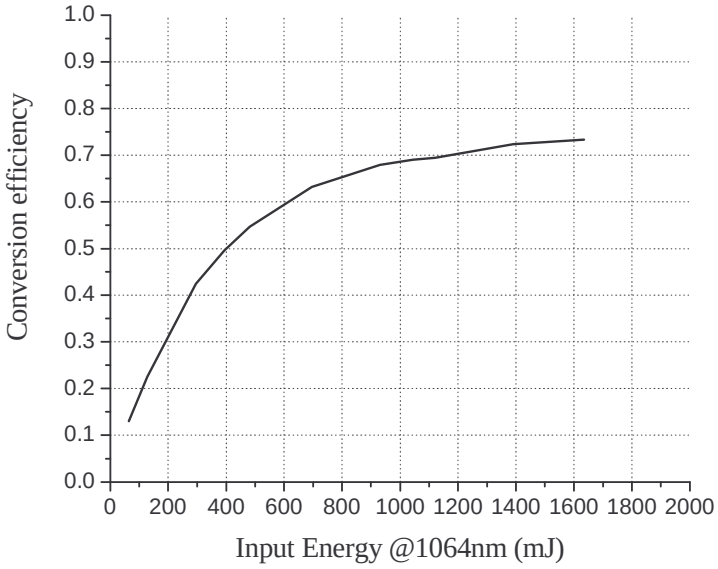

Figure 3.18: Second harmonic generation conversion efficiency from 1064nm to 532nm through a 14mm×14mm×4mm KTP type II crystal with a collimated beam.

The expanded beam goes through a thin film polarizer that selects the Stokes pulse of the SBS phenomenon. Following the thin film polarizer is a quarter wave plate to create circular polarization. A focusing lens with 60cm focal length is chosen to control the complete overlap inside the SBS cell and ensure the optimum reflectivity and compression. The SBS is realized in a 80cm cell with a diameter of 9.5cm filled with FC-72. This fluorinert liquid is constantly circulating (except during experiment) through a filtering system with a pore size of 25nm to prevent any particules that would create breakdown during the focusing process.

The compressed Stokes generated by SBS phenomenon, is phase conjugated of the fundamental, and maintains the same circular polarization. Going through the quarter wave plate again rotates the polarization to vertical, this polarization is reflected by the thin film polarizer. The complete system for the SBS compression (thin film polarizer, quarter wave plate, lens, SBS cell, lens ,quarter wave plate, thin film polarizer) operates with 80% efficiency. The spectrum obtained from a Fabry-Perot interferometer shows an increase of the spectral bandwidth and a shift in the wavelength (fig. 3.19), an indication of phase conjugaison and compression of the pulse. We now have a 300ps, 2J, 532nm laser beam.

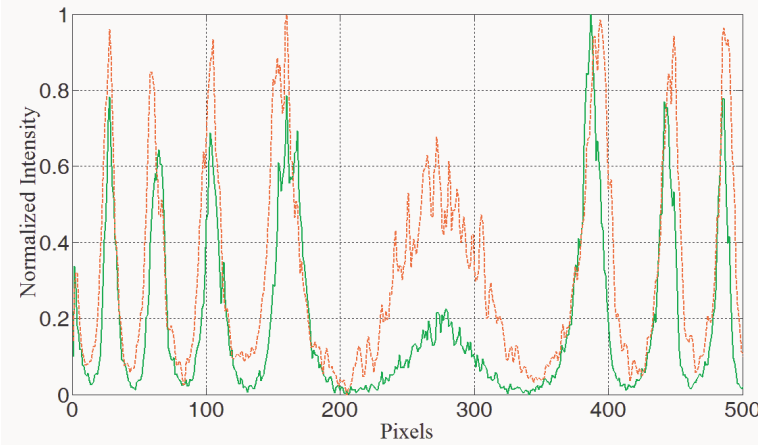

Figure 3.19: Full line: spectral bandwidth of a beam taken from a classical mirror Dotted line: spectral bandwidth of a beam taken after the SBS cell. The mirrors of the Fabry-Pérot have a 88% reflectivity and are separated by 60mm.

The compressed beam is sent to the fourth harmonic generation crystal, which is placed at the same distance from the thin film polarizer as the output coupler of the cavity to the thin film polarizer. As the beam is phase conjugated this allows to reconstruct a flat top beam and compensates for the defects due to the beam propagation. The fourth harmonic crystal is a KDP type I crystal with the following dimensions: 50mm×50mm×5mm.

Considering the second harmonic reduction of pulse length This make us believe that the compression is of a factor 10. Considering the second harmonic reduction of pulse length we can conclude that the generated pulse is about 250ps. The global setup of the laser can finally be summarized by the figure 3.20.

We finally at the end of the laser system achieve a flat top beam profile at 266nm with a pulse duration of 250ps and an energy up to 500mJ that corresponds to a peak power of 2GW. This power is about 50 times more than the critical power for filamentation at this wavelength (cf Chapter 2).

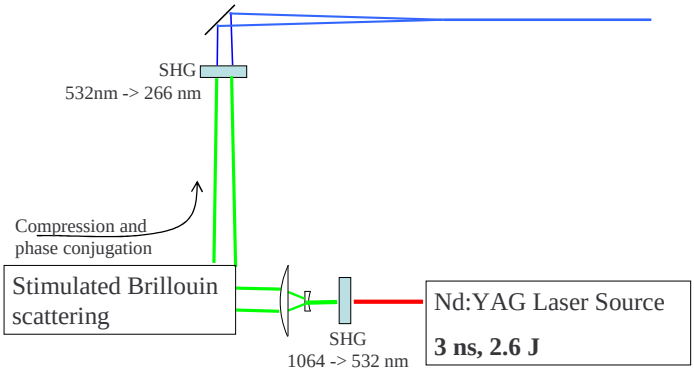

Figure 3.20: Diagram of the full laser setup to produce short UV pulse.

Chapter 4

Experimental Observation of Filament

In this chapter, we present the first experimental observation of long pulse - high energy - filaments, and compare the results to the theoretical predictions

4.1 Filamentation

To make an accurate measurement of the distance of propagation of the filaments we need to know their starting point. To do so a new tool as been developed. We will in this part explain this tool and present the results obtained.

4.1.1 Aerodynamic window

Launching the Filaments

As explained before, a laser beam of very high power (P>36MW) can collapse during its propagation in a small spot size and keep this size for a rather long distance. The sensitivity of the nonlinear effect initiating this propagation to perturbation, small fluctuation of power and beam profile makes it impossible to predetermine where

the filament will start along the beam path. A first solution investigated was to use a long focal length to favor a starting point. This technique improves slightly the accuracy, but does not solve the ambiguity between filamentation propagation and the moving focus.

The best evidence of filament is obtained by launching a beam in air with the energy and shape of the non-diffracting beam calculated in Chapter 2. As the media in our case is simply air the problem is to create this initial conditions at a particular location. The theory and computer simulation are telling us that our beam should present a power higher than the critical power and a size of the order of a few hundreds of micron. The problem seems easy to solve. Let us focus the beam in vacuum and then go in the air! Then come the problem of the interface between air and vacuum. If a glass window is used, it will be blown up by the very high intensity of the beam at this location.

A tool "recycled" from the high power CO_2 laser era of the 60's is used to answer the question: the aerodynamic window. The designed piece of equipment allows a supersonic flow of air to travel through it. Its shape create a Venturi effect that creates the vacuum in one side of the flow of air and the atmospheric pressure on the other side (figure 4.1). The supersonic flow of air acts as a valve between the vacuum and the atmospheric pressure. Two holes offering passage for the laser beam can be drilled at those two locations. The incoming laser beam sees first the vacuum, then a laminar supersonic flow of air for a very small distance, and finally the ambient atmospheric pressure.

The use of this tool fixes the starting position of the filament and resolve the problem of the moving focus. The focus being inside the vacuum or just at the interface with air, the nonlinear effect cannot project this focus backward or foward by Kerr lensing effect. Figure 4.2 is a picture of the disassembled aerodynamic window. One can see on the left of the design a narrow nozzle. It is through this nozzle that the supersonic flow of air is generated, provided a pressure of 3atm can be maintain upstream of the nozzle. On the right is the expansion cchamber.

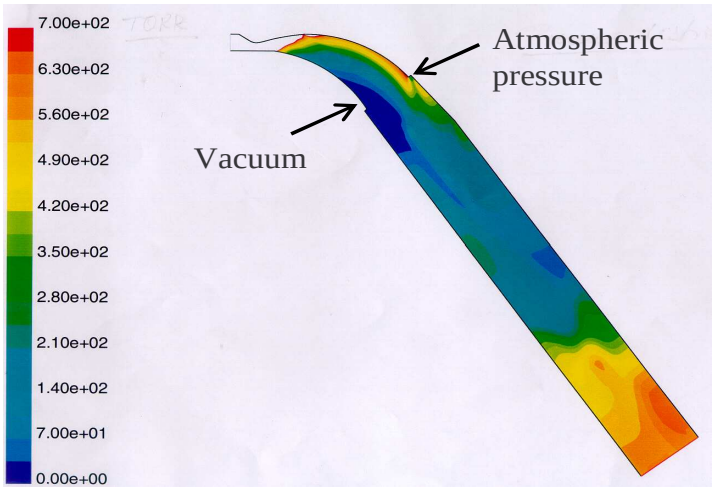

Figure 4.1: Distribution of the pressure into the aerodynamic window.

A 3m long vacuum tube is connected to the low pressure hole of the aerodynamic window, as shown in Fig. 4.3. The vacuum formed in the tube is of about 87Torr. With external pumping, a pressure of 37Torr is reached. The aerodynamic window is run continuously during the measurement of filaments.

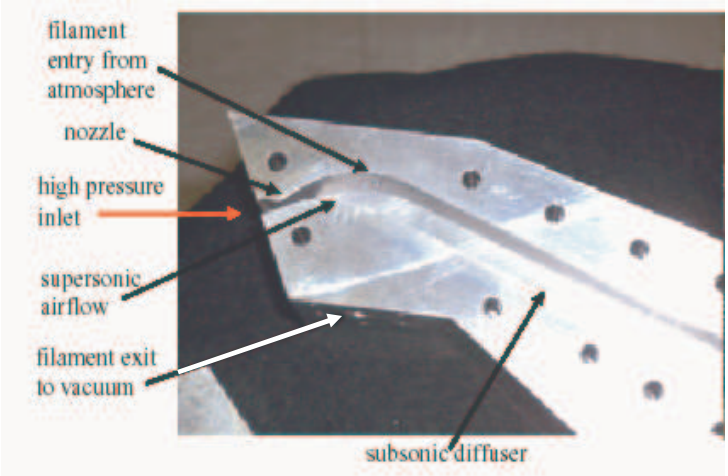

Figure 4.2: Picture of an aerodynamic window open.

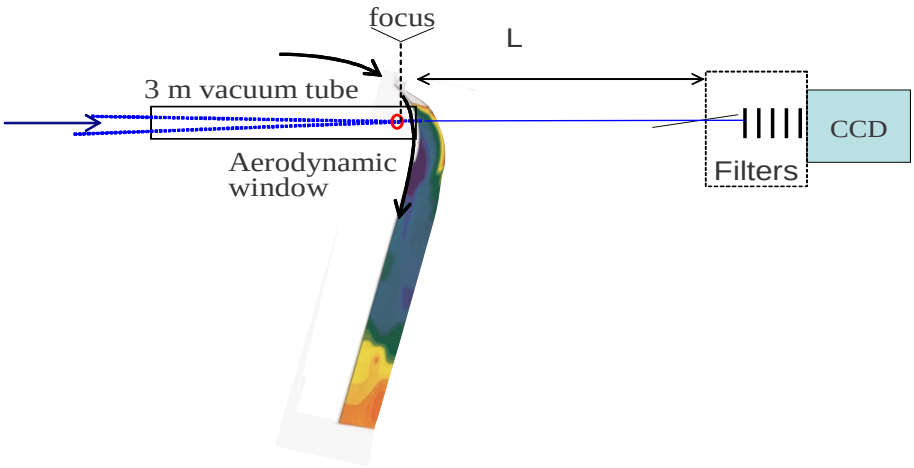

Figure 4.3: Setup for observation of filament starting point: vacuum tube 3m long focus of the beam before the window, aerodynamic window and propagation of the beam. diagnostic system with grazing incidence plate and filter before the CCD. Distance of propagation of the filament L.

Diagnostics

A similar dilemma as encountered in the previous paragraph arises when attempting to perform measurements on filaments: how to make a diagnostic without damaging all the optics. One could consider using again an aerodynamic window, in which the filament would enter from the atmospheric pressure side, and let to diffract in the vacuum. Unfortunately, since the filament size is expected to be close to 1mm (cf. Chapter 2), it would take a propagation length of several tens of meter in vacuum before the diffracted beam size reaches 1cm, and linear attenuation can be used.

An alternate technique is used to attenuate the filament down to intensity levels at which transmission filters can be used. It consists in reflecting most of the filament energy with a thin plate of fused silica at grazing incidence. The plate is only 1mm thick, in order to prevent nonlinear effects in fused silica to distort the filament profiles. The beam transmitted through the thin plate is further attenuated by two 45^o high reflectivity mirrors used in transmission. Fine tuning of the attenuation is performed with neutral density filters put in front of the CCD.

Configuration of measuring UV filaments

As detailed in Chapter 3, the phase conjugated beam retro-reflected by the Brillouin cell is 3,5cm in diameter, and focuses at 5.6m. The last 3m of focusing takes place in a vacuum tube, terminate by an aerodynamic window. The detection discussed in the previous paragraph is located at a distance L from the aerodynamic window (Fig. 4.3). The CCD used for the experiment presents a pixel size of 8.3μm and give picture in false color proportional to the intensity of the beam. The attenuation system in front of the camera tend to give some fringes on the pictures. Those picture are then filtered with a Matlab program to reduce the contrast of those fringes.

This setup allowed us to make a direct measurement of the filament and beam profile at different positions from the aerodynamic window. The measurements have been realized from 1.5m up to 4.5m away from the aerodynamic window. A closer measurement was not possible due to the small size of the surrounding beam around the filament creating to much intensity and damaging the optics. A longer measurement was not possible either due to size of the laboratory.

The light rejected from the second high reflectivity mirror was send through a spectrometer to analyse the spectrum generated from the filament propagation.

4.2 Observation of UV filaments

The focal spot size is 100μm at the aerodynamic window. The Rayleigh range corresponding to w_0=50μm is 3cm. At a distance L=3m from the aerodynamic window, the beam should have expanded to 1.9cm , which is indeed the observation at low intensity. Figure 4.4 shows on the left the beam filling the CCD due to the geometrical diffraction at a power lower than the critical power, after a distance of propagation of 1.50m.

As the power is raised there is a sudden collapse of the beam. Additional filters in front of the camera are required to record the new beam size (center picture in

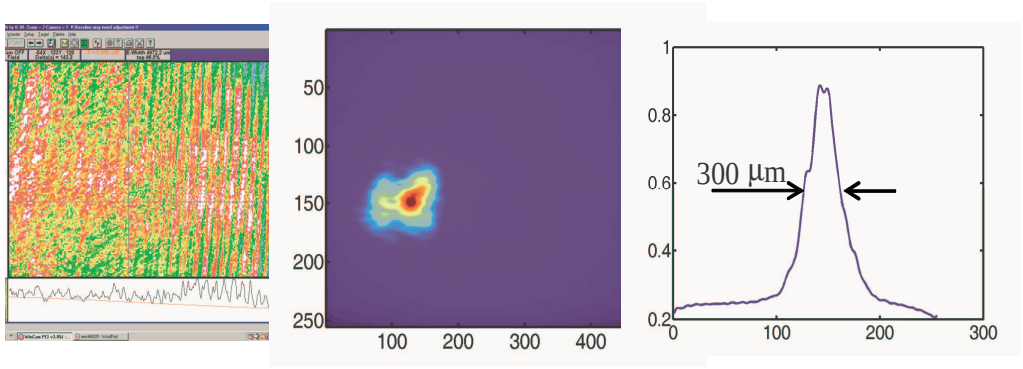

Figure 4.4: Left: P<P_{CR} no filamentation the beam diffract according the geometrical optic. Right: P>P_{CR} Picture of a filament after 1.50m of propagation after the aerodynamic window.

Fig. 4.4). A plot of a cut through this profile, shown on the right, indicates a diameter (FWHM) of 300μm. Better instrument would be required to make a quantitative fit of the experimental profile to the theory (cf Chapter 2).

Figure 4.5 shows the filament after 2m of propagation. Those filaments measurements were obtained with the aerodynamic window in operation. Some test have been realized with the aerodynamic window off (no vacuum). The result of this experiment was a less probable generation of filaments and moreover the filaments formed were presenting a bigger diameter. An example is shown on Fig. 4.6. This shows the interest of the aerodynamic window not only to get a fix starting point for filamentation but moreover to prevent the losses during the self-focusing of the beam which can prevent the filament formation. The amount of energy necessary to form filament with the aerodynamic window allows also to observe single filaments and not a multiple filamentation like classically observed in the infra-red.

The filaments observed have a waist of about 400μm, which is smaller than the one predicted by the theory (600μm Chapter 2). This could be explained by the pulse duration of the beam at the origin of the filament. The model is developed for pulse between 2ns and 175ns to be on a steady state regarding the density of electron. As the pulse in our experiment is of only 200ps the steady state for the density of electron is not yet reached. The density of electron being lower than the

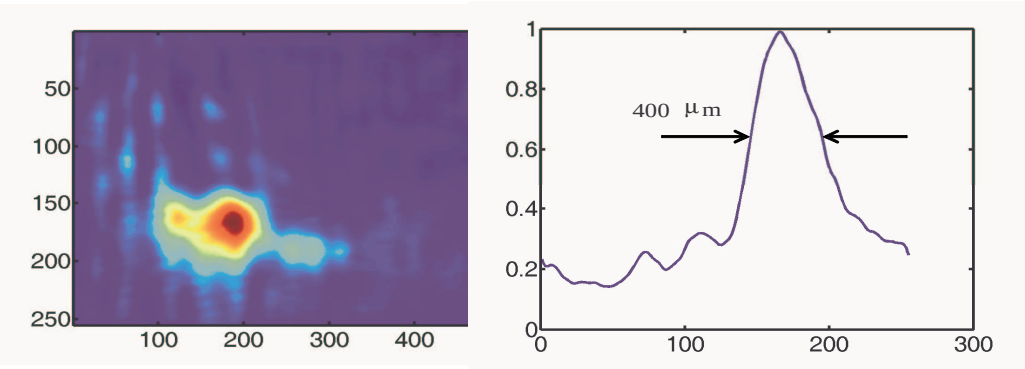

Figure 4.5: Picture of a filament after 2m of propagation after the aerodynamic window.

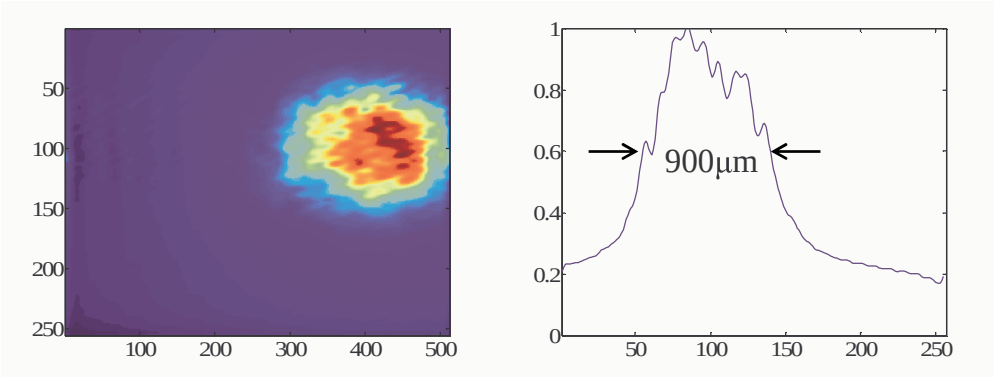

Figure 4.6: Picture of a filament after 2m from the aerodynamic window position reference. The starting point cannot be determined.

equilibrium density the beam has therefore to focus down to a smaller diameter in order to be sensitive to the plasma defocusing when the intensity reaches a higher value. The 400μm waist obtained experimentally can be explained for this reason in comparison of the theoretical value.

It should be noted that the beam size at the aerodynamic window is only 100μm, hence much smaller than the expected filament size. According to the theory it should not be possible to create a filament under those conditions but the presence of other factors not taking into account in the model might help for the formation of the filament. Those factors are the Raman scattering loss, the Rayleigh scattering loss and maybe some others...

The theory in Chapter 2 showed that the filament is an oscillation between self-

focusing and -defocusing which makes the beam size fluctuates with a certain periodicity of the order of several meters. Those oscillations could not be observed due to the limiting size of the laboratory.

In parallel of the observation of the filament profile, a measurement of the spectrum was realized as explained before. Spectral components were observed at 283.6nm, 303.6nm, 326.7nm, 353.7nm and 385.4nm. The Raman shift of the nitrogen being $\Delta\nu = 2330cm^{-1}$ we concluded that the spectral bands come from the the Raman scattering generation of the N_2 during the propagation. Up to the fifth Stokes is observed which can bring the question of the amount of loss due to Raman scattering during the propagation of the filament.

Chapter 5

Conclusion and Future Work

5.1 Summary of the Work Done

The theory developed several years ago, predicted that a scaling up of the nonlinear propagation of UV pulse was possible. This theory, along this work, as been revisited and corrected to take more accurately into account phenomenon that are taking place, such as the attachement of the electrons.

This propagation model predicts a stable propagation for a beam having a waist of 600μm and a power of 495MW. This model highlight the fact that the nonlinear propagation is an equilibrium between the self-focusing of the beam by Kerr effect, and the self-defocusing by the plasma formation. Oscillation along the path of the beam between those two phenomenon can be seen. Moreover the propagation is predicted to be able to go on for very important distance (the order of the kilometer), despite the losses due to the multiphoton ionization.

This study has been complimented by a search for steady state solutions for the propagation model in collaboration with the mathematics department of the University of New Mexico. In this approach, losses are neglected. Using the ionization coefficient as a parameter, a family of steady state solutions is found. Starting from the well known "Townes soliton", evolving toward a Gaussian shaped profile with

the same beam diameter and power as found through the first method.

The experimental part of this work consisted in a development of a laser source to verify this theory. This laser source consists in a Nd:YAG laser delivering 3ns, 2.6J pulses at a wavelength of 1064nm. The pulses are frequency doubled to achieve 2J at 532nm. The pulses are phase conjugated and compressed using stimulated Brillouin scattering in FC-72. Finally the beam is frequency doubled for the last time to produce 200ps, 500mJ pulses at 266nm.

A new tool for the diagnostic of the filament, the aerodynamic window, was used to conduct the experiment on the beam. Its interest on the formation and the control of the filament has been proven by this experiment.

We have been able to observe filament from long UV pulses propagating on the length available in the laboratory (4m). This distance represents 100 time the Rayleigh range. Those filaments present a beam waist of about 400μm which agrees with the theory and the models previously developed considering that the pulse duration of our laser is shorter than the time required to reach a steady state.

5.2 Future Work

The future work is still quite vast. On the theory, two major things can be including in the next step: first the Rayleigh scattering can be introduced as a loss of power during the propagation of the filament; second the Raman effect from N_2 occurring during propagation has to be taken into consideration. Moreover further investigation have to be done to find stable solution of the models when the initial beam phasefront presents a radius of curvature, or when the critical beam size is less than 150μm.

On the experimental point of view, observation of up to the fifth Stokes of the Raman generation from N_2 molecules has been observed during our experiment. This phenomena has to be further investigated. Then, off axis imaging of the filament has to be done and also observation of the filament using a streak camera. An upgrade

of the laser can be also realized to have more freedom and control on the initial conditions of the beam. Another set can be reached by upgrading the laser, which is to have enough energy to achieve filamentation without the need of pulse compression by stimulated Brillouin scattering. This would allow study of the filament in the physical conditions consistent with the theoretical model.

The plasma formed by the filament is of a rather short lifetime. To sustain this conductor channel open an exciting radiation has to be added. Alexandrite laser at 750nm can deliver easily high energy long pulse that will keep the plasma excited and prevents its recombination. The long pulse UV filament can now be used in correlation with Alexandrite laser to trigger electric discharge. And finally, with a little monetary help a laser at 290nm or 307nm could be developed and tested. The choice of those two wavelength is made by their "easy" accessibility and by the very low loss from Rayleigh scattering that they encounter during their propagation in the air but also because they still involve only a three photon process to ionize the oxygen.

Appendix A

Laser Induced Breakdown Spectroscopy

In this annex we will present some work realized with this laser for another project. The subject of this project was to identify explosive residus on a target at a remote distance. We use to do so the technique of laser induced breakdown spectroscopy (LIBS).

A.1 Experimental Setup

The principle of this experiment is to focus a intense laser beam on a target. The high intensity of the beam ejects some particles at the surface of the material and create a plasma at this surface. The emission spectrum of the plasma created at the surface is dependant on the material present at this surface. Classically a set of strongly focusing lenses allows to collect the emitted light close to its origin in a fiber optic which then go to a spectrum analyser for treatment. It implies also to have a strongly focusing lens to create the plasma with an off the shelf laser. Due to their rather "low" power those lasers need a tight focus to reach a high enough intensity to involve the research phenomenon. Those problems make this technique to be not as remote as desired. The interest of our laser is in this part.

As the laser as a high power it doesn't need a tight focus to create the plasma. So a 5m focal length lens allows to create plasma on any given materials. Moreover In the case of filamentation their is no need of a focusing lens and as the beam propagates, under those conditions, for a very long distance the target can be place far away from the source. This solve the problem of the distance laser source-target but the problem target to diagnostic system is still present. We have solved this problem by using an off-axis parabolic mirror with a long focal length that focuses the light emitted by the plasma to a remotely placed spectrometer.

We are able using this setup to realize a spectrum analysis of a target placed at 6m from the laser and the spectrometer is also at 6m from the target. A more remotely test could be done but we were limited by the size of the laboratory. The amount of light collected from the target was bright enough to expect a system with at least two times the distance previously used.

At the output of the spectrometer was placed a CCD camera which allowed us to record a 50nm spectrum at a time.

A.2 Results

Different experiments have been made using this system to prove its efficiency. First of all, due to the interest of the project we tried to compare the results obtained from a low power laser beam focused on the target and the results obtained using a filament. No difference have been seen for the 266nm laser wavelength which approve our idea that filament could be used in the same way as focused beam for laser induced breakdown spectroscopy. Moreover the distance limitation of this technique is increased to the distance of propagation of the filament (several kilometers according to the filamentation theory). The following results are obtained using filamentation but with the size of the lab the same results were obtained using tight focus.

Then different substrates have been tested at different wavelengths. Figure A.1 presents the results of the spectra obtained from aluminium and copper substrate

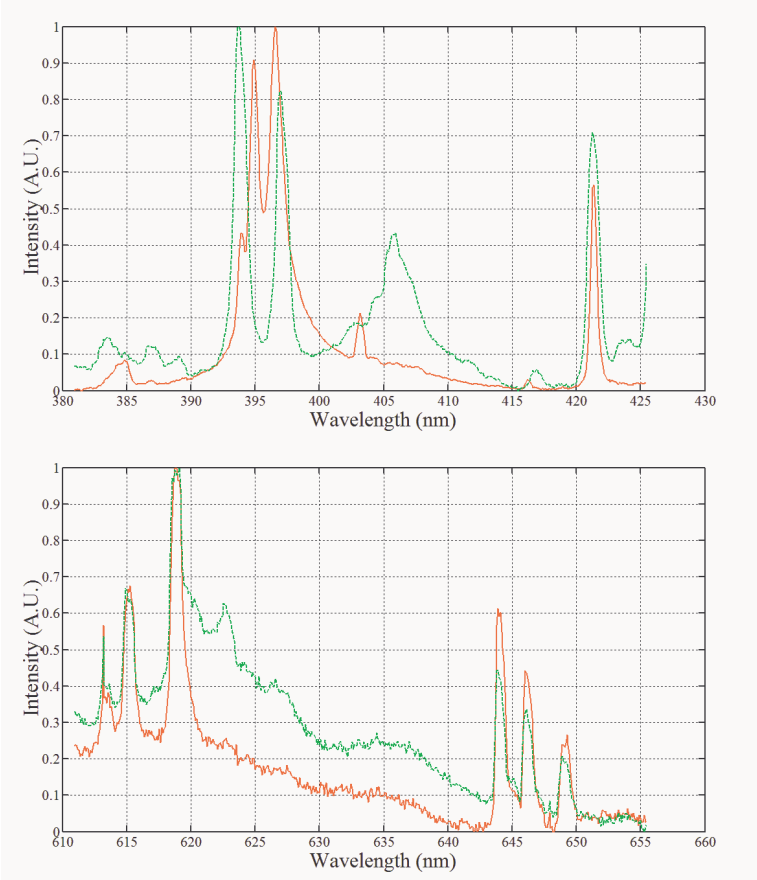

Figure A.1: Dotted lines: Spectra of Copper obtained by LIBS with filaments, Full lines: Spectra of Aluminium obtained by LIBS with filaments

from 375nm to 425nm and from 610nm to 660nm.

The final interest of this project was to find if it is possible to detect explosive residus on the substrates. We are showing in figure A.2 the results obtained with two completely different type of explosive constituents. The explosives are either based on carbon-nitrogen bound like DNT, TNT and RDX or on nitrogen-chlore bound like in ammonium perchloride. If those two bound could be detected by our technique a majority of the explosives could be detected as well.

The C-N bound classically emits at 388nm and for the N-Cl bound it is detectable at 635nm. We can see on the figure A.2 that the C-N bound at 388nm is clearly identify on the substrates when DNT is deposited. The N-Cl bound is also detected at 635nm from the substrates covered with ammonium perchloride. We can con-

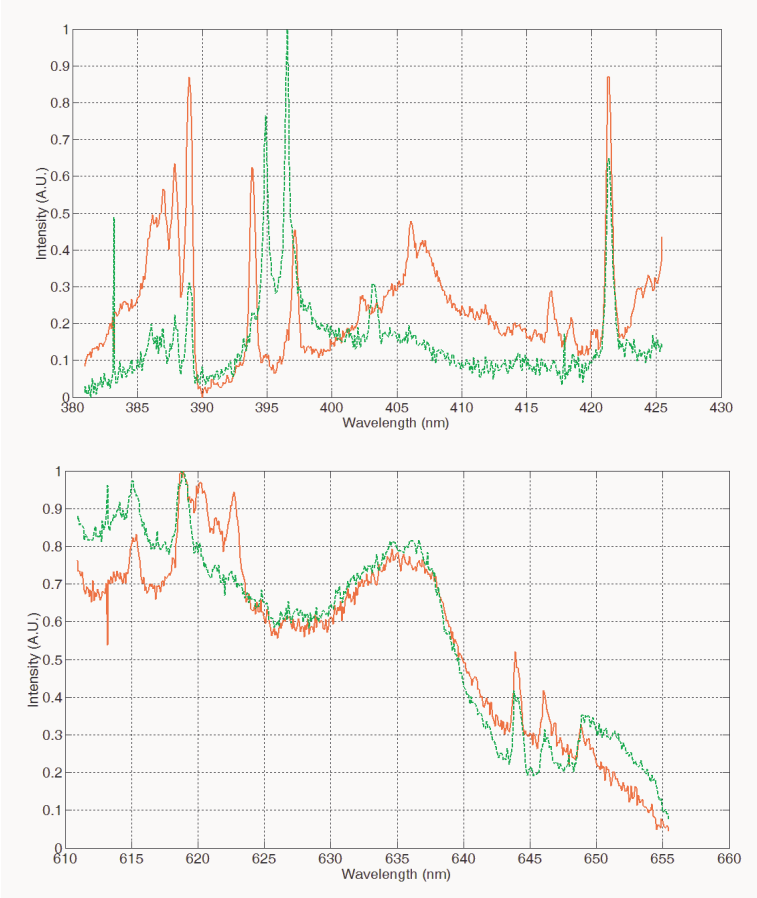

Figure A.2: Top: Dotted lines: Spectra of DNT on Copper obtained by LIBS with filaments, Full lines: Spectra of DNT on Aluminium obtained by LIBS with filaments, Bottom: Dotted lines: Spectra of ammonium perchlorate on Copper obtained by LIBS with filaments, Full lines: Spectra of ammonium perchlorate on Aluminium obtained by LIBS with filaments,

clude that our spectroscopy measurement to identify explosives using filament, is a convenient way for a far remote detection system.

Appendix B

Numerical Values

B.1 Plasma characteristic field calculation

The coefficient of the term in the square root in the definition Eq. (2.46) of the characteristic field is:

$$\frac{e^2 c}{2m_e\omega^2} = \frac{(1.602\cdot 10^{-19})^2 \times 3\cdot 10^8}{2\times 9.108\cdot 10^{-31}\times (7.0863\cdot 10^{15})^2} = 8.4169\cdot 10^{-32}\mathrm{C^2LT/K}. \quad \text{(B.1)}$$

The square root term in Eq. (2.46) is:

$$\sqrt{\frac{\sigma^{(3)}N_0}{2\eta_0\beta_{ep}n_0}} = \sqrt{\frac{3.\cdot 10^{-41}\times 5.46897\cdot 10^{24}}{2\times 377\times 1.3\cdot 10^{-14}}} = 4.09125\cdot 10^{-3}\mathrm{T/CV^2}. \quad \text{(B.2)}$$

The product:

$$8.4169\cdot 10^{-32}\times 4.09125\cdot 10^{-3} = 3.4436\cdot 10^{-34} \quad \text{(B.3)}$$

has indeed the units of $C^2LTTV/(CV^3K) = CVLT^2/(KV^3) = L^2T^{-2}LT^2/V^3 = L^3/V^3$.

B.2 Critical power

The expression for the critical power is:

$$P_{cr} = \frac{\lambda^2}{8\pi n_0\bar{n}_2} = \frac{(0.266)^2\cdot 10^{-12}}{8\pi n_0\times 7.8\cdot 10^{-23}} = 36.1\mathrm{MW}. \quad \text{(B.4)}$$

Parameter	Symbol	Defined through:	Value	Units
Self focusing susceptibility	$\chi^{(3)}$	$=2n_0n_2$	$2.07 \cdot 10^{-25}$	m^2/V^2
Self focusing index (field)	$\bar{n}_2$	$=\epsilon_0 c n_0 \bar{n_2}/2$	$1.035 \cdot 10^{-25}$	m^2/V^2
Self focusing index (Intensity)	$\bar{n}_2$	measured	$7.8 \cdot 10^{-23}$	m^2/W
Critical power	P_{cr}	$\frac{\lambda^2}{8\pi n_0 \bar{n}_2}$	$3.61 \cdot 10^7$	W/m^2
Recombination coefficient	β_{ep}		$1.3 \cdot 10^{-14}$	m^3/s
Attachment coefficient	γ		$1.5 \cdot 10^8$	s^{-1}
Oxygen density	N_0		$5.46897 \cdot 10^{24}$	m^{-3}
Three photon absorption	$\sigma^{(3)}$		$3.0 \cdot 10^{-41}$	m^6s^2/J^3
Charact. field for self-foc.	$\mathcal{E}_0$	$\sqrt{\frac{\eta_0}{\bar{n}_2}}$	$2.198 \cdot 10^{12}$	V/m
Wavelength	λ		266	nm
Distance normalization	k	$\frac{2\pi n_0}{\lambda}$	$2.362 \cdot 10^7$	m^{-1}
Light angular frequency	ω	$2\pi c/\lambda$	$7.086 \cdot 10^6$	radian/s
	$1/\mathcal{E}_c^3$		$3.0444 \cdot 10^{-34}$	m^3/V^3
Charact. field plasma defoc	$\mathcal{E}_c$	Eq. (2.46)	$1.4266 \cdot 10^{11}$	V/m
Coefficient a	a	$(\mathcal{E}_0/\mathcal{E}_c)^3$	$3.657 \cdot 10^3$	

Table B.1: Various nonlinear parameters of air at 266 nm

What is the relation between P_{cr} and $\mathcal{E}_0$? The intensity corresponding to the characteristic field is:

$$I_0 = \frac{\mathcal{E}_0^2}{2\eta_0} = \frac{(2.198 \cdot 10^{12})^2}{2 \times 377} = 6.407 \cdot 10^{21} \mathrm{W/m^2}. \tag{B.5}$$

We note that the critical power corresponds to the characteristic intensity $\mathcal{E}_0^2/(2\eta_0)$ over a normalized cross-section of $\chi^2 = \pi$. At 266 nm, $\sqrt{P_{cr}/I_0} = 0.075\mu$m, and $\chi = k \times 0.75 \cdot 10^{-7} = \sqrt{\pi}$.

B.3 Order of magnitude of the normalized field

There are two conditions to be satisfied: the power should exceed the critical power for self-focusing defined by Eq. (B.4), and the field should be such that the self-focusing balances defocusing. The last conditions implies:

$$\mathcal{E}_r \approx \frac{1}{a} \tag{B.6}$$

which implies

$$\mathcal{E} \approx \frac{\mathcal{E}_c^3}{\mathcal{E}_0^2} = 6. \cdot 10^8 \mathrm{V/m}. \tag{B.7}$$

This field corresponds to an intensity of $6.13 \cdot 10^{14}$ W/m^2. The ratio of the critical power to this intensity yields a cross section of $0.589 \cdot 10^{-6}$ m^{-2}, or (0.8 mm)^2. This corresponds roughly to the 800 μ diameter observed in numerical simulations. As dimensionless radius, we would choose $\chi = 18000$.

References

[1] A. Becker, N. Aközbek, K. Vijayalakshmi, E. Oral, C. M. Bowden, and S. L. Chin. Intensity clamping and re-focusing of intense femtosecond laser pulses in nitrogen molecular gas. *Appl. Phys. B*, 73:287–290, 2001.

[2] D. W. Koopman and T. D. Wilkerson. Channeling of an ionizing electrical streamer by a laser beam. *J. Applied Physics*, 42:1883–1886, 1971.

[3] A. Sukhinin and A. Aceves.

[4] S. Smith L. Branscomb, D. Burch and S. Geltman. Photodetachment cross section and the electron affinity of atomic oxygen. *Phys. Rev.*, 111(2):504–513, 1958.

[5] M. Yamaura. Improvement of the atmospheric discharge laser-triggered ability using multiple pulses from a kilohertz krf laser. *J. Appl. Phys.*, 98, August.

[6] R. Hegerberg and R. W. Crompton. Diffusion, attachment and attachment cooling of thermal electrons in oxygen and oxygen mixtures. *Aust. J. Phys.*, 36:831–844, 1983.

[7] J. Schwarz, P. K. Rambo, J.-C. Diels, M. Kolesik, E. Wright, and J. V. Moloney. Uv filamentation in air. *Optics Comm.*, 180:383–390, 2000.

[8] J. Schwarz and J.-C. Diels. Analytical solution for uv filaments. *Phys. Rev. A*, 65:013806–1—013806–10, 2001.

[9] L. V. Keldysh. Ionization in the field of a strong electromagnetic wave. *Soviet Physics JET*, 20(5):1307–1314, 1965.

[10] M. A. Biondi. Recombination. In G. Bekefi, editor, *Principles of Laser Plasmas*, pages 125–157, New York, 1976. John Wiley & Sons.

[11] A.W. Ali. The eelectron avalanche ionization of air and a simple air chemistry model. *NRL Memorandum Report*, 4794, 1982.

[12] R. Geballe M.A. Harrisson. *Phys. Rev*, 91(1), 1953.

References

[13] Miles V. Klein and Thomas E. Furtak. *Optics*. John Wiley and Sons, ISBN 0-471-87297-0, New York, 1986.

[14] T.D. Grow, A. A. Ishaaya, L. T. Vuong, A. L. Gaeta, R. Gavish, and G. Fibich. Collapse dynamics of super-gaussian beams. *Optics Express*, 14:5468–5475, 2006.

[15] V. Etuhov and A. E. Siegman. Twisted-mode technique for obtaining axially uniform energy density in a laser cavity. 4.

[16] A. Yariv and D.M. Pepper. Amplifief reflection, phase conjugation, and oscillation in degenerate four-wave mixing. *Optics Letters*, 1(1):16–18, July.

[17] V.V. Ragul'skii F.S. Faizullov B.Ya. Zel'dovich, V.I. Popovichev and P.N. Lebedev. Connection between the wave fronts of the reflected and exciting light in stimulated mandel'shtam-brillouin scattering. *ZhETF Pis. Red.*, 15(3):160–164, 1972.

[18] V. Kmetik, H. Yoshida, H. Fujita, M. Nakatsuka, and T. Yamanaka. *Advanced High-Power Lasers*.

[19] H. Yoshida, V. Kmetik, H. Fujita, M. Nakatsuka, T. Yamanaka, and K. Yoshida. Heavy fluorocarbon liquids for a phase-conjugated stimulated brillouin scattering mirror. *Applied Optics*, 36:3739–3744, 1997.

[20] E.S. Fry. Visible and near-ultraviolet absorption spectrum of liquid water. *Applied Optics*, 39(16):2743–2744, June 2000.

[21] C.G. Freeman T.I. Quickenden and R.A.J. Litjens. Some comments on the paper by edward s. fry on the visible and near-ultraviolet absorption of liquid water. *Applied Optics*, 39(16):2740–2742, June 2000.

[22] E.S. Fry. Reply to criticisms of the pope and fry paper on pure water absorption maed in a comment by quickenden et al. *Applied Optics*, 39(31):5843–5846, November 2000.

[23] J.A. Irvin T.I. Quickenden. The ultraviolet absorption spectrum of liquid water. *J. Chem. Phys.*, 75(8):4416–4428, April 1980.

[24] K. Kuwahara, E. Takahashi, Y. Matsumoto, S. Kato, , and Y. Owadano. Short-pulse generation by saturated krf laser amplification of a steep stokes pulse produced by two-step stimulated brillouin scattering. *J. Opt. Soc. Am. B*, 17(11):1943–1947, 2000.

[25] V. Kmetik, H. Fiedorowicz, A. A. Andreev, K. J. Witte, H. Daido, H. Fujita, M. Nakatsuka, and T. Yamanaka. Reliable stimulated brillouin scattering compression of nd:yag laser pulses with liquid fluorocarbon for long-time operation at 10 hz. *Applied Optics*, 37(30):7085–7090, 1998.

[26] V. Kmetik, T. Kanabe, H. Fujita, M. Nakatsuka, and T. Yamanaka. Optical absorption in fluorocarbon liquids for the high energy stimulated brillouin scattering phase conjugaison and compression. *The review of laser engineering*, 26(4):322–327, 1998.

[27] E. Albrecht, G. Baum, T. Bellunato, A. Bressan, S. Dalla Torre, C. D'Ambrosio, M. Davenport, M. Dragicevic, S. Duarte Pinto, P. Fauland, S. Ilie, G. Lenzen, P. Pagano, D. Piedigrossi, F. Tessarotto, and O. Ullaland. Vuv absorbing vapours in n-perfluorocarbons. *Nuclear Ins. & Met. in Phys. Res. A*, 510:262–272, 2003.

[28] Iavor T. Veltchev. *Stimulated Brillouin Scattering Pulse Compression and Harmonic Generation: APPLICATIONS TO PRECISION XUV LASER SPECTROSCOPY*. PhD Dissertation, June 2001.

[29] J.-P. Huignard A. Brignon, editor. *Phase Conjugate Laser Optics*. Wiley Interscience, 222 Rosewood Drive, Danvers, MA, 1st edition, 2004.

[30] W.A. Neuman C.B. Dane and L.A. Hackel. High energy sbs pulse compression. *IEEE Journal of Quantum Electronics*, 30(8):1907–71915, August 1994.

References

.